

Dynamics, Analysis and Experiments of Obstacle Negotiation for Wheeled Mobile Robots

Mathew Kfourri

Department of Mechanical Engineering
McGill University

August 15, 2024

A thesis submitted to McGill University in partial fulfillment of the requirements of the degree of

Master's of Mechanical Engineering

©2024 Author

Abstract

Hybrid wheel-leg robots combine the high efficiency of wheeled locomotion with the obstacle negotiation abilities of articulated suspension. Effective performance indicators are needed as optimization goals for both mechanism design and trajectory planning to take full advantage of the abilities of these robots. This work investigates the concept of admissible kinetic energy and related performance indicators to develop a framework for obstacle negotiation analysis, design, and control. A four wheeled-legged robot is used as a test platform to analyze the suite of performance indicators based on velocity and joint position, and predict which wheels are in contact at the moment of impact. A physical test platform including current sensors, encoders and an accelerometer was designed and constructed to validate the simulation results. A dynamic model of the test platform constructed for impact analysis is validated through a combination of high-speed camera measurements, force measurements and current sensing. Selected performance indicators based on admissible kinetic energy are shown to influence the ability of this vehicle to negotiate an obstacle, with and without accounting for the configuration dependent effect of traction.

Résumé

Les robots hybrides roues-jambes combinent l'efficacité de locomotion sur roues avec les capacités de négociation d'obstacles de suspension articulée. Des indicateurs de performance efficaces sont nécessaires comme objectifs d'optimisation pour la conception des mécanismes et planification de trajectoire. Ce travail étudie le concept de l'énergie admissible et les indicateurs de performance associés pour améliorer l'analyse, la conception et le contrôle de la négociation d'obstacles. Un robot à quatre roues et jambes a été utilisé comme plateforme de test pour analyser la suite d'indicateurs de performance basés sur la vitesse et prédire quelles roues sont en contact au moment d'impact. Une plateforme de tests physiques incluant des capteurs de courant, des encodeurs et un accéléromètre ont été conçus et construits pour valider les résultats de simulation. Un modèle dynamique de la plateforme construite pour l'analyse d'impact est validée par un combinaison de mesures par caméra à grande vitesse, de mesures de force et détection de courant. Indicateurs de performance sélectionnés basés sur l'énergie admissible influencent le capacités de ces robots à franchir un obstacle, tout-seul et en tenant compte de l'effet de traction dépendant de la configuration.

Acknowledgements

I am grateful to a wide variety of individuals and institutions who were vital in allowing this work to exist. I would like to thank the rest of the Advanced Dynamics Lab for their insightful discussions and the use of the Multibody Dynamics Library. Special thanks goes to Anya Forestell and Michael Farquarson whose advice and camaraderie made this project significantly more enjoyable, and to Alex Coulombe for his electrical wisdom. Thank you to Elizabeth Beauclair for her love, support and award-worthy camera work. Heartfelt thanks to my parents and grandfather, who inspired me to both start and finish this project. My deep appreciation to Professor Higgins and Taj Sobral, whose help and patience in lending the use of a high speed camera and a space to film in was vital to the existence of this project. I gratefully acknowledge the support of the Natural Sciences and Engineering Research Council of Canada (NSERC), CM Labs Simulations Inc, and the Canadian Space Agency (CSA). Finally, I would like to thank my supervisor Professor Kövecses for years of guidance and insight.

Contents

1	Introduction	1
2	Literature Review	3
2.1	Obstacle Negotiation	3
2.2	Problem Statement	4
2.2.1	Stability	5
2.2.2	Collision Avoidance	6
2.2.3	Mobility	6
2.2.4	Dynamic Obstacle Negotiation	8
3	Design and Construction of a Test Platform	10
3.1	Objectives and Constraints	10
3.1.1	Reconfigurable suspension	10
3.1.2	Ease of testing	11
3.1.3	Measure changes in kinetic energy	12
3.1.4	Common design components	12
3.2	Conceptual Design	13
3.3	Design Embodiment	15
3.3.1	Suspension Actuators	15

3.3.2	Structure dimensions	16
3.3.3	Drive system	17
3.3.4	Motor controllers	18
3.3.5	Force sensors	18
3.3.6	Data acquisition system	19
3.3.7	Computer/Microcontroller	19
3.3.8	Power	20
3.4	Detail Design	21
3.5	Solid Model Construction and Validation	22
4	Calculation of Performance Indicators	24
4.1	Dynamic Model	24
4.2	Impulse-Momentum Formulation	25
4.3	Determination of Active Constraints	27
4.4	Admissible Velocity Calculation	29
4.4.1	Selected Performance Indicators	30
4.5	Energy Analysis of Obstacle Negotiation	32
5	Results	34
5.1	Configuration Optimization	34
5.2	Active Contact Prediction	37
5.3	Motion Analysis Experiments	41
5.3.1	Motion Analysis Setup	41
5.3.2	Motion Analysis	42
5.4	Full Maneuver Experiments	45
5.4.1	Experimental Setup	45

5.4.2	Performance Analysis	47
6	Conclusion	54
6.1	Suggestions for Future Work	55
A	Design Calculations	62
A.1	Joint Actuators	62
A.2	Slope Driving	64
A.3	Stress Analysis	65
A.3.1	Differential Shaft	66
A.3.2	Finite element analysis	67
A.4	2D Force Sensor	69
B	Design Drawings	71
B.1	Machine Drawings	71
B.1.1	Frame Parts	71
B.1.2	Suspension	73
B.1.3	Modular Motor Mounts	76
B.2	Current Sensor Circuit	78
B.3	Main Body Layout	79
B.4	Electrical System Diagrams	81

List of Figures

3.1	Quadruped Design Inspirations	14
3.2	Test Platform Models	22
4.1	LCP Diagram	26
4.2	Admissible Velocity Diagram	31
5.1	Diagram of robot with joint labels and origin lines	36
5.2	Optimized Robot Configurations	36
5.3	Robot in low admissible configuration contacting an obstacle	37
5.4	Analysis of contact with 30° obstacle	39
5.5	Analysis of contact with 25° obstacle	40
5.6	Photron capture setup	42
5.7	Summary of corrected kinetic energy	43
5.8	Tracking of low T_a configuration	46
5.9	T_a measurement summary	48
5.10	T_{a-COM} measurement summary	52
5.11	T_{a-ul} measurement summary	53
A.1	Diagram of rover at full extension	62

A.2	Diagram of rover bodies at full extension	64
A.3	Simplified robot climbing slope at constant speed	65
A.4	Differential load case	66
A.5	Suspension attachment FEA	67
A.6	Shoulder link FEA	68
A.7	Bicep link FEA	68
A.8	Free body diagram of robot between elbow joint and ground	69
B.1	Frame bracket	71
B.2	Long frame bar	72
B.3	Short frame bar	72
B.4	Spacer for pillow-block mounting	72
B.5	Frame-differential attachment plate	73
B.6	Differential shaft extension	73
B.7	Suspension attachment member	74
B.8	Shoulder link	74
B.9	Upper load cell link	74
B.10	Load cell attachment plates	75
B.11	Lower load cell link	75
B.12	Large actuator spacer	75
B.13	Small actuator spacer	76
B.14	Adjuster motor mount	76
B.15	Actuator attachment plate	77
B.16	Rear actuator attachment plate	77
B.17	Current sensor circuit diagram	78
B.18	Component diagram-Main level (mm)	79

B.19 Component diagram-Upper level (mm)	80
B.20 Electrical system overview	81
B.21 Data collection system	82
B.22 Drive system	82
B.23 Actuator system	83

List of Tables

3.1	Test platform design summary	11
3.2	Servo choice summary	16
5.1	Summary of generated configurations	36
B.1	Electrical component list	80

Chapter 1

Introduction

Navigation on rough terrain in off-road environments is a difficult and complex problem for a wide range of vehicles, both manned and unmanned. In this terrain, obstacle negotiation ability is often the limiting factor for the operational range of a mission, and incorrectly predicting obstacle navigability can result in a vehicle being stuck temporarily or lost completely. Obstacle negotiation is the process of traversing a segment of terrain that is significantly rougher, steeper, or more uneven than the surrounding terrain.

As the use of autonomy and teleoperation continues to expand, fast and accurate techniques for prediction of navigation ability become even more critical. At the same time, mobile robots, and ground vehicles in general, are increasingly taking advantage of more cost effective processing power and electrical actuation to add additional degrees of freedom to their suspensions with the aim of improving performance. Increasingly articulated suspension also expands the space of design and planning options, which in turn requires a higher degree of sophistication from the analytical tools used in the design process.

This work concerns the development and empirical validation of a set of performance indicators based on the concept of admissible and constrained motion, and their associated

admissible and constrained kinetic energies. These performance indicators consider explicitly the inertial effects of the onset of contact with an obstacle, and attempt to predict a vehicle's obstacle negotiation ability on hard terrain. A test platform is designed and constructed to demonstrate the effectiveness of the calculated performance indicators. The research is organized as follows:

Chapter 2: A background on obstacle negotiation is presented. Common strategies for assessing three sub-problems in obstacle negotiation: stability, collision avoidance and mobility, are outlined.

Chapter 3: The design process for construction of a robotic test platform is described, from design goals and constraints to production drawings and electrical schematics. Major design decisions and component choices are justified.

Chapter 4: A dynamic model used for simulation of the robot is assembled and discretized at the Impulse-Momentum level. A linear complementarity problem (LCP) is set-up and solved to identify active contacts at the moment of impact. The set of active contacts is used to isolate the subspace of admissible motion from which the set of performance indicators is derived.

Chapter 5: Experimental setups for direct velocity measurement, LCP validation and obstacle negotiation assessment are described. Results from each set of experiments are presented and their support for the assumptions made in Chapter 4, as well as the effectiveness of the calculated performance indicators are assessed.

Chapter 6: The work is concluded with a review of major objectives achieved and suggestions for future work.

Chapter 2

Literature Review

2.1 Obstacle Negotiation

Vehicle obstacle negotiation is the process of crossing a segment of terrain that is significantly rougher, steeper, or more uneven than the surrounding terrain. This maneuver is considered successful when the center of mass of the vehicle is brought past the highest point of the obstacle [1].

A vehicle's obstacle negotiation performance is commonly measured by comparing the diameter of its wheels to the largest vertical step it can climb [2]. A vehicle not designed for obstacle negotiation can generally climb steps of a height up to half the diameter of its wheels. Mobile robots equipped with passive rocker-bogie suspension, such as NASA's Mars rover Curiosity, can climb steps equal in height to the diameter of their wheels [3]. Rovers equipped with other passive mechanisms such as EPFL's Shrimp robot have demonstrated step climbing abilities of up to 2 times the wheel diameter [2]. Active mechanisms such as the wheel-legged robot PAW can climb steps up to 2.25 times the wheel diameter while remaining in contact with terrain throughout the maneuver [2].

An alternative measure of obstacle negotiation ability can be obtained by measuring the steepest slope a vehicle can traverse in a given terrain type, or by comparing the slip ratios required to negotiate a given slope [4]. The RCP, a 6 wheeled rocker-bogie rover test platform can negotiate a slope of 11° maximum by default, with a 22.5kg payload [5]. The SherpaTT wheel-legged rover can negotiate slopes up to 28° on a terrain of loose soil and duricrust using active re-configuration [3]. NASA's Spirit and Opportunity rovers were able to negotiate slopes up to 30° on hard Martian soil, which is now a requirement for Mars rover missions, but were nearly immobilized on similar slopes consisting of looser soil [6].

2.2 Problem Statement

Consider some vehicle with an arbitrary number of contact points between its wheels and the terrain. Its acceleration at a given moment will be fully defined by a sum of all contact and friction forces at each contact point, and the effect of gravity [7]. A vehicle with active suspension can negotiate an obstacle by shaping contact forces to satisfy a desired trajectory [7]. The normal contact forces and the positions of wheel-ground contact points can be directly controlled, depending on actuator capability and the range of motion of the vehicle suspension. The contact points and forces are additionally subject to two terrain constraints. First, the normal components of the contact force vectors must remain non-negative, as it is assumed that there is no adhesion between the contact points and the terrain [7]. Second, the tangential forces are limited by friction. This limit is generally modeled by Coulomb friction for hard terrain or derived from empirical data or finite element analysis for soft terrain [7, 8].

In vehicles with passive or underactuated suspension, the contact points and forces are largely determined by a combination of vehicle and terrain geometry. Therefore, obstacle

negotiation ability is primarily determined at the design stage, where obstacle negotiation models can be used to develop vehicle geometry and suspension topology of desired capability across a range of terrain [9].

Coupling between these various requirements as well as uncertainty in terrain measurements makes the planning or design problem difficult to solve directly. Instead, it is often separated into three requirements for successful traversal: stability, mobility, and collision avoidance, often using proxies when direct evaluation is inconvenient or impossible [2].

2.2.1 Stability

Stability in a vehicle can be interpreted as its ability to produce a desired motion without requiring adhesion at any of its contact points [7]. Often, an unstable vehicle will tip over, but contact loss at a wheel does not always indicate loss of stability as the vehicle may still be able to produce a net force in the desired direction of motion.

In general a vehicle is stable if the desired net force f_{ig} intersects the “convex hull” i.e. the minimum area polygon created by joining each contact point projected onto a plane perpendicular to the resultant force [10, 11]. If the resultant force vector does not intersect this polygon, then the vehicle is unstable and the target resultant force vector cannot be created from valid (i.e. non-adhesive) contact forces. Stability can then be measured using a distance d between the intersection point and the closest edge of the polygon, or the smallest angle θ between f_{ig} and any displacement r that joins the COM and a contact point [10]. An energy stability margin (ESM) can be used instead which measures the amount of energy required to lift the COM to the point that f_{ig} intersects the edge of the support polygon i.e. to the point of tipping [2]. This measure allows comparisons between different vehicles, and measures resistance to disturbances by taking into account both the vehicle mass and COM

height.

2.2.2 Collision Avoidance

Possible unintended points of contact need to be predicted and then implemented as geometric constraints during a control or design optimization, to insure that contact between vehicle and terrain is only at intended locations [11]. In the case of a step obstacle, the likeliest collision point is the corner of the step [2]. Distance between the vehicle edges and the step corner can be calculated explicitly to prevent collisions. Some vehicles have suspension geometry such that no mechanical components exceed the dimensions of the wheelbase, making collisions when traversing a slope unlikely. However, for vehicles with a high degree of reconfigurability, any section that overhangs the front or back set wheels must be checked for collisions at the intended onset of contact of that set of wheels.

2.2.3 Mobility

Mobility in the context of obstacle negotiation is the ability of a vehicle to produce enough net force to move in a desired direction, subject to maximum friction forces. Often, mobility will be calculated assuming constant speed and zero acceleration, known as quasi-static assumptions [2]. These assumptions hold when the nominal vehicle speed is low and constant, resulting in minimal acceleration due to rotations during obstacle traversal. Quasi-static assumptions may also prove sufficient to control a faster moving system provided the control loop speed operates even faster, as the errors caused by acceleration between time steps will be minimal.

Mobility may be determined using the static conditions for continued movement at critical points, i.e. where traction is predicted to be the lowest, in each stage of crossing an obstacle

using the Newton-Euler equations [1, 11]. Then, a range of feasible configurations can be obtained by substituting in the relevant friction and geometric constraints, from which an optimal configuration and required motor commands can be calculated. This approach requires multiple points of analysis specific to every robot-obstacle combination and has been demonstrated using both Coulomb and terramechanics models to predict maximum friction force [1, 11].

In certain cases verifying the mobility of a vehicle directly as outlined above is undesirable or impractical. This may be due to the range of obstacles and terrain the vehicle intends to traverse, uncertainty as to terrain or vehicle characteristics, or computational complexity in cases of many contact points and a mechanically complex vehicle. Critical points may also be difficult to identify before analysis begins, or a control strategy is required for the moments between critical points. Instead, performance indicators, measurements that have been shown to correlate with mobility or traction, can be used.

Some examples of mobility performance indicators include the ratio between the normal contact force and the tangential contact forces at a contact point, and the angle between the normal of the contact plane and tangent plane of the wheel at that point. [7, 12]. Both of these indicators can be used to predict the quality of the contact at a given point, with higher values reducing the amount of slip generated for a given amount of traction [9]. The contact point positions used for calculation of the support polygon can be shifted away from low quality contact points, resulting in a single metric indicative of both mobility and stability [12]. Other performance indicators, such as normal force dispersion, combine the effect of all the contacts into a single metric by measuring the standard deviation of the normal forces at each wheel-terrain interface from one another [8]. Reducing the difference between the normal forces at each wheel reduces the slip required to produce the same drawbar pull for a vehicle. This metric was however only validated on flat terrain.

2.2.4 Dynamic Obstacle Negotiation

Little previous work attempts to predict the effect of momentum and contact-related momentum changes on obstacle negotiation, which tends to be ignored in low speed maneuvers. Nevertheless, some investigators have seen that vehicle momentum can have a significant effect on obstacle negotiation performance. In the case of a hybrid tracked robot, a higher approach speed was found to result in a smoother and more stable gap crossing and improved slope-climbing ability despite an increase in initial contact force [13].

In the area of vehicle dynamics, especially for trucks where high weight and speed increases the significance of momentum, the relationship between slope navigation and initial velocity has undergone some investigation. Consider that a heavy trucks' maximum steady-state speed on an uphill slope is generally limited by engine power, and their minimum steady-state speed on a downhill slope is limited by brake friction and heat dissipation [14]. Both the slope angle and initial speed, as well as the vehicle mass have been shown to influence the time and distance it takes to reach that steady-state speed, which in turn limits the navigable slope grade [15]. However, existing simulations often only predict the vehicle's motion after it begins climbing or descending the slope, which ignores the influence of the initial contact [14]. For the purpose of vehicle design and planning, it is useful to be able to predict how much additional momentum will aid in obstacle negotiation, and how this is affected by different vehicle parameters, such as wheelbase size and weight distribution. Though some research has shown that lowering the center of mass of the vehicle improves dynamic negotiation ability, little has been done to answer this question systematically [16].

As the applications of robotic vehicles expand to missions that can make use of higher speeds, considering inertial effects becomes critical [17]. A set of indicators based on the concept of admissible velocity of a vehicle remaining after contact with an obstacle have been

proposed to take advantage of these dynamic effects. Using the mass matrix of the vehicle, and geometric information about the obstacle, the momentum conserved after contact can be predicted. Admissible velocity-based indicators can then predict if the vehicle will travel up a slope immediately after contact, information that cannot be obtained from static traction analysis [17]. This work intends to demonstrate that the kinetic energy associated with this admissible velocity can be used to directly predict the performance of a vehicle on a sloped obstacle, and as an optimization goal for design and control. No other performance indicators have been identified in this literature review that intend to predict obstacle negotiation ability directly from starting configuration.

Chapter 3

Design and Construction of a Test Platform

3.1 Objectives and Constraints

The goal of this design process is to create, within eight months, a robot suitable for testing a variety of obstacle negotiation techniques and performance indicators. Based on this primary objective, four design sub-goals were chosen, then developed into additional constraints to guide the design process. These requirements and constraints are summarized in Table 3.1, and elaborated on below.

3.1.1 Reconfigurable suspension

The robot must have highly reconfigurable suspension to be able to provide data on test runs with a wide variety of performance indicator values. Performance may be influenced by any number of factors including the mass and inertia of the robot, as well as the arrangement of contact points. Therefore, the suspension should be sufficiently actuated to allow the

Objectives	Associated Requirements
Reconfigurable suspension	≥ 2 degrees of freedom per limb
	Large range of motion
Ease of testing	Lightweight
	Compact
	Centralized data collection
	Drive current sensors
	IMU
	Joint encoders
Measure changes in kinetic energy	Moderate top speed
	Contact force sensors
Common design components	Wheel-legged suspension
	Lockable differential
	Modular steering

Table 3.1: Test platform design summary

contact point locations to change without moving the main body or vice versa. Additionally, a large enough range of motion is required so that the effect of differences in configuration is large enough to be measured. A reconfigurable suspension, even if not used actively during negotiation, can act as a proxy for the effect of design changes that would require mechanical alterations in a non-reconfigurable robot.

3.1.2 Ease of testing

To optimize its ease of use as a test platform, the robot must be lightweight and compact to store, and be able to record sufficient data to compare the performance of sets of training runs. To both assess the effect of traction and identify the moments of impact this instrumentation should include current sensors to identify the work done by the drive wheels, and an inertial measurement unit (IMU) to measure the orientation and acceleration of the robot's main body. Encoder measurements for all actuated joints are

needed to verify the actual robot configuration at any moment. The data should be recorded on board and easily collected to optimize turnaround time between tests.

3.1.3 Measure changes in kinetic energy

The robot must have the ability to measure moderate changes in kinetic energy. This requires drive motors that reach a sufficiently high speed so that moderate differences in kinetic energy after impact (i.e. admissible kinetic energy) are detectable. Including contact force measurements can be useful to corroborate measured changes in admissible kinetic energy. This is possible as contact force has been associated with constrained kinetic energy, and the robot initial kinetic energy can be fully decomposed into admissible and constrained kinetic energy [18]. Therefore, higher constrained kinetic energy should indicate lower admissible kinetic energy. Contact force measurements are also used in many other obstacle negotiation strategies, and can be useful for future experiments and to compare the measured weight distribution to simulated values [8].

3.1.4 Common design components

As the goal of this test platform is to demonstrate the effectiveness of various obstacle negotiation techniques, it should include major design components similar to other mobile robots used commercially or in research. This should allow the effect of the obstacle negotiation strategies to be clear, compared to the effect of a novel design. A wheel-legged suspension design would make this test platform comparable to research robots such as Hylos [19] or commercial concepts such as Schaeffler's Dex [20]. A lockable suspension differential also improves performance on uneven terrain and allows comparison to a class of mobile robots with both passive and active suspension such as the platform developed

by Jiang et al [21]. Modular steering motors allow the test platform to optionally execute more complex maneuvers and more closely model wheel-legged robots such as Dex, or the independent steering of deployed Mars exploration rovers.

3.2 Conceptual Design

With the design objectives and constraints defined, the overall robot layout and major components can be chosen. Where multiple options appeared viable, the preferred alternative was chosen based on projected cost and overall construction time. To satisfy the reconfigurable suspension requirements, the design options for the overall robot form factor were narrowed down to 4 wheeled vehicles with active suspension. This wheel choice allows possible application to the very large class of non-robotic 4-wheeled vehicles and avoids the higher cost and complexity of a larger number of wheels. Knowing that a large suspension range of motion is desired eliminates the Mars exploration rover style vehicles from consideration. Their active suspension derives from the deployment motors located near the wheels which only allow one degree of freedom per wheel. The remaining possible vehicle layouts can be organized into three categories with examples shown in Fig. 3.1: (a) without steering, (b) with steering and (c) with steering and adjustment motor.

The three robots displayed in Fig. 3.1 were developed for very different purposes: low cost education, research, and search and rescue, yet have fundamentally similar suspension limb designs. Each limb has two independently controlled degrees of freedom with axes parallel to the ground and perpendicular to the front of the robot. (a) has no steering motors, though it can skid steer by adjusting the relative speed between the left and right wheel. The cheapest and least complex way to add steering is to add a third suspension actuator on each limb perpendicular to the ground as in (b). However, this limits the configuration space

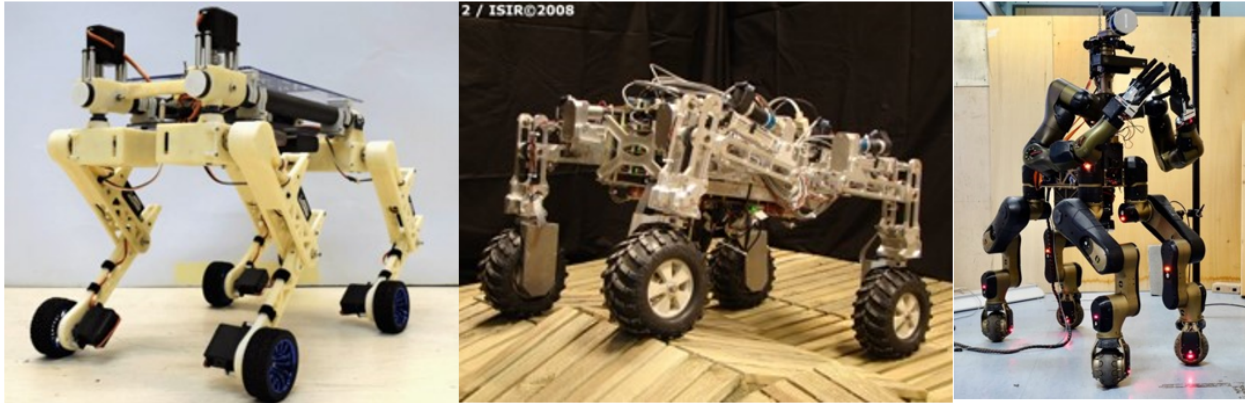


Figure 3.1: (a) No steering [22], (b) Steering [19], (c) Steering and adjustment [23]

where steering will be effective. As the suspension moves and the steering axis becomes less perpendicular to the ground, caster increases, increasing the actuator torque required and making the direction of travel more difficult to predict. This problem can be solved using additional actuators to keep the steering axis perpendicular to the ground as the suspension moves, as in (c). However, additional actuators incur significant costs and complexity. A robot using steering and adjustment motors will have nearly twice the number of actuators required for version (a). Passive solutions using pulleys, such as the one developed for Creadapt can keep the angle between the steering and robot body constant, but significantly increase the mechanical parts required for construction [24].

As many obstacle negotiation techniques developed in the literature consider two-dimensional models, it was decided that a robot limited by a lack of steering (a) would be worth the reduction in time and cost gained by omitting additional actuators. Therefore, configuration (a) is selected. However, steering attachments will be designed to be added as optional modules in case steering is required for a future project.

3.3 Design Embodiment

As is common to most design problems, certain design choices must be made iteratively due to complex interactions between various robot systems. In this case, general metrics such as overall robot weight and size were predicted in advance, to allow possible motor and frame materials to be chosen. Then, as more components are specified, the estimates are updated, and any affected components are re-verified to ensure feasibility. The following design embodiment is presented using final dimensions.

3.3.1 Suspension Actuators

Joint actuation is commonly performed by either linear or rotary actuators. Linear actuators have a high strength to weight ratio, and so are commonly chosen as shown in Fig. 3.1 (a) and (b). However, the high range of motion requirement eliminates them from consideration. For simplicity, suspension joints are commonly actuated using servomotors. Constructed from a compact combination of brushed or brushless DC motor, encoder and control circuit, servos can move to a given position in response to a single control command. Purchasing motors and encoders separately is possible and can give more control to the designer while sometimes reducing costs, but is generally less compact and requires significant extra mechanical and electrical complexity and design time. Standard commercially available servos, while able to perform internal position control, have no way of sending encoder values back to the control computer. As joint position measurements are a design requirement, ‘smart’ servos were selected instead, that can transmit position, speed and temperature as needed.

The load case for each suspension joint must be determined before actuator selection continues. Detailed derivation is in Appendix A. This load case was determined for the robot at its widest stance, where load on each joint is predicted to be highest. As most

Joint	Stall Torque Requirement (Nm/kgf.cm)	Dynamixel Servo Cost (\$)	HerkuleX Servo Cost (\$)
Shoulder	6.47/66.0	545	466
Elbow	3.29/33.6	350	382
Adjustment	1.65/16.8	155	214
Steering	1.65/16.8	155	214
Total (4 limbs)	-	4820	5104

Table 3.2: Calculated torque requirements

servos are advertised in stall torque instead of operating torque, the results of the load case analysis were converted into required stall torque using the maximum power point (half of the stall torque) as maximum torque.

Only two brands were able to supply smart servo actuators with a stall torque of at least $67.3Nm$: HerkuleX and Dynamixel. Mixing different servo brands is not preferred due to the difficulty of implementing multiple communication systems for servo control. As can be seen from the table above, the two systems have very similar costs, with the HerkuleX based system being about 5% more expensive. As rotation speed (about 60 RPM) and mounting ability (tapped holes on front and rear faces) were also nearly identical, the HerkuleX servo set was chosen due to a more user-friendly communication protocol and library.

3.3.2 Structure dimensions

The joint lengths, i.e. distance between elbow and shoulder or elbow and drive axes of rotation is limited by two factors. Its minimum is constrained by the servo length, 57mm, which must lie fully within the link to prevent restriction of the range of motion. Its maximum is constrained by the maximum acceptable torque of the servos, translating to 109mm for the upper arm and 150mm for the lower arm. Exceeding these lengths would require a more expensive and larger servo. A joint length of 100mm was chosen, to keep the links the same

length and includes an extra 10% margin for servo strength error. To easily fit within the previously determined space constraints, the base must be less than 50cm x 50cm. Otherwise, it only need be large enough to contain all necessary electrical components, and long enough to allow significant rotation of the elbow joints. This layout is shown in Appendix B.

3.3.3 Drive system

The drive system must be able to propel the robot fast enough that kinetic energy based performance indicators become significant, while staying within the test range of about 3m. Traversing this distance in one second (not considering acceleration and deceleration) is chosen as a maximum speed, as any malfunction at a higher speed would be difficult to control. The motors should also be capable of propelling the robot up slopes up to 40° so that drive motor torque is not the limiting factor for any obstacle negotiation techniques. Continuous servos were considered, but none were identified that could run fast enough in combination with a wheel radius less than the joint length in a feasible price range. A DC brushed motor with built in encoder is the next most compact and simple to control option. As both wheel size and gearbox effect the output torque and speed values, a desired power is calculated for use in motor choice, in this case approximately 20W. Wheel size and gearbox can then be altered to get the desired torque and speed. A detailed calculation is found in Appendix A. A combination of a 9cm diameter wheel and 612rpm HD Planetary gearmotor with encoder is chosen to fulfill these requirements. Larger wheels and a different would also gearbox also fulfill the design requirements. However, a wheel radius larger than 50mm would require restriction of the range of motion of the steering actuators when present, to prevent collision with the elbow link.

3.3.4 Motor controllers

The chosen DC brushed drive motors require motor controllers that can supply up to 12V of power at a maximum current of 10A, the current draw per motor at the maximum power point. Sabertooth dual 12A 6V-24V DC motor drivers were chosen for this purpose as they are compatible with a Kangaroo motion controller. This motion controller attaches to the motor driver, receives data from the encoders and performs auto tuning of an internal proportional-integral-differential (PID) controller. It can then enact position or velocity commands in response to a serial input, transforming the motor-driver-controller combination into a servo like system.

3.3.5 Force sensors

Force sensors are integrated in the lower limb section to allow contact force measurement during traversal. 6 axis force-moment sensors would give the most complete picture of loads during operation, but are outside the budget of this project. They also tend to be supplied with large and heavy data acquisition systems. It is possible to acquire stress and strain data using strain gauges directly, and construct a circuit to combine the signals from multiple strain gauges into a full set of force-moment data. This option was discarded due to design time constraints, and concerns about the likely sensitivity of a handmade circuit to perturbations on a mobile robot. Instead, a single axis tension-compression force sensor was used, with a full scale range of 200N and maximum error of 0.2%. Though not able to measure the full set of contact forces, combined with encoder measurements for angle identification it can measure contact forces in the plane of the wheel as is demonstrated in Appendix A. These measurements are sufficient for all 2-D based obstacle negotiation techniques. Friction forces in the plane of the wheel can be measured through analysis of

current sensor data.

3.3.6 Data acquisition system

Force sensors and current sensors output analog signals at very low voltages. These signals require amplification as well as conversion into digital values to be recorded and stored by a computer system. High value was placed on ease of use when searching for an applicable system, as constructing a bespoke data acquisition system can involve writing detailed firmware and design and printing of circuit boards, which is outside the scope of a mechanical engineering project. The Sparkfun family of Qwiic products was identified as a possible solution. The Qwiic system is a set of breakout boards that use 4-pin JST connectors to power and communicate with one another through I2C. These boards come with firmware that allows them to be immediately recognizable once connected to a master board. The Artemis board is an example of a master board, chosen in this case for its data acquisition capabilities. This board can connect to a computer through a USB-C port and record data from connected sensors to an internal SD card slot. It additionally has an integrated IMU.

3.3.7 Computer/Microcontroller

A microcontroller or onboard computer is required to coordinate and control the robot's various systems. A wide range of options are available, from microcontrollers such as Arduinos or Teensys to small form factor computers such as a Raspberry Pi or Nvidia Jetson. The primary design criteria for the microcontroller is the ability to connect to all required devices. With two drive motor controllers, two chains of servos and a data acquisition system, at least 5 UART or USB ports are required. The only microcontrollers

identified that satisfy this requirement are the Arduino Mega and the Arduino Portenta-H7. The Arduino Mega's processor, a 16MHz ATmega2560 with 256kb of flash memory caused it to be removed from consideration due to low speed and memory which may limit the robot's capabilities, especially if online trajectory adaptation is later desired. The Portenta's processors, and ability to be connected to a display give it strong reasons for selection, but high cost (\$168) bring it into competition with mini computers such as the Raspberry PI 4 8GB (\$104) and the Jetson Nano (\$300). The Raspberry PI is selected for its combination of low cost, and the wider availability of support for hardware projects compared to the then newly released Portenta and less common Jetson Nano.

3.3.8 Power

Ease of use requirements for the test platform require it to be used in moderately confined space indoors. This allows the option of a wired connection to an off-board power supply as opposed to an onboard battery. An off board power supply has the advantage of reducing rover weight, loosening the servo torque requirements, and is often cheaper for a given current requirement. It does however introduce some additional error due to dragging wires that are difficult to model precisely. A battery will more closely represent a deployed robotic systems, but requires frequent recharges depending on capacity and additional voltage regulators to ensure a consistent voltage source. To fulfill ease of testing requirements a wired power supply was chosen.

Identification of an appropriate power supply requires assessment of the maximum required current of the robot, as well as the most common supply voltage. The most significant power draw will be the drive motor and joint actuators. The joint actuators need to be driven at up to 14V, and the drive motors, though optimized for 10-12V can be connected to a controller running at 14V. Capping the drive speed at 85% will ensure the

drive motors are not run above 12V and do not need an additional voltage regulator to create a 12V supply. Considering the measurement range of the current sensors and the projected operating points of the drive motors, they are fused at 5A each, requiring a total maximum of 20A. The joint actuators, after communicating with the manufacturer, require 3A fuses, which limits the possible total current draw to $3 \times 8 = 16A$. The only other significant source of power consumption is the control computer, which requires 2.1A at 5V. The load cells and data acquisition system require a mix of 5V and 3V3, but at low enough current draw that they can be powered indirectly through the Raspberry Pi.

To limit the amount of required voltage converters, a power supply that can output 14V power supply is chosen. A 30A max current supply was chosen, as one that could supply the total $20 + 16 + 2.1(5.1/14) = 36.7A$ would be considerably more expensive. It is similarly unlikely that the drive and adjustment motors will be running at maximum power at the same instant. Subsequent testing supports this decision, as no crash-free experimental run resulted in insufficient power, which can be detected by the main computer crashing when voltage drops below 5V.

3.4 Detail Design

A mechanical structure is needed to connect all major components chosen in the design embodiment. Major considerations for this design include sufficient rigidity such that the system's flexibility does not need to be considered in subsequent analysis, low lead time, and weight limited by actuator capabilities. Strength at predicted critical points is assessed using finite element analysis or hand calculations in Appendix A. A complete mechanical design and an assembled view of the default (without steering) configuration shown in Fig. 3.2. Bounding boxes and nominal weights are used for electrical components, with actuators



Figure 3.2: a) SOLIDWORKS model b) Assembled test platform

and wheels modeled using manufacturer supplied models. All structural parts are made from flat aluminum or extruded 90°aluminum, which can be water-jet cut, reducing lead time. A complete set of machining drawings, electrical bill of materials and components layout can be found in Appendix B.

3.5 Solid Model Construction and Validation

Mechanical parts with rigid connections to one another were grouped together into links, resulting in a total of 17 rigid bodies. The SOLIDWORKS model is used to calculate the mass and inertia properties of each link, as well as the displacement between each joint axis of rotation and link centers of mass. This information is input into a MATLAB based model and forward dynamics simulation using the Multibody Dynamics Library developed by the Advanced Dynamics Lab at McGill University. This library was altered to correct the implementation of non-penetration constraints referred to as 'Wall' constraints. These constraints were combined with rolling constraints and a Coulomb friction model to

represent unilateral contact constraints by switching between rolling and sliding during wheel-terrain interaction. The MATLAB simulation is used primarily for calculation of performance indicators from the dynamic model and for a visual representation of the negotiation manoeuvre; it is not intended for detailed modelling of the contact itself between wheel and obstacle.

The test platform's mass was measured and compared to the total weight of the model, to account for extra wires and hardware not included in the SOLIDWORKS representation. This difference was used to correct the mass and inertia properties of each link. Final validation of the mass properties and link lengths was performed by measuring the normal force on the robot's front and back wheels in 3 different joint configurations and comparing the results to the MATLAB simulation. This yielded an average error of 1.51%, showing a high degree of alignment between physical vehicle and model.

Chapter 4

Calculation of Performance Indicators

The performance indicators detailed in this paper are dependent on the parameters and dynamic model of the vehicle of interest as well as the obstacle geometry at the onset of contact. This vehicle dynamic model is presented and also developed for an impulse-momentum formulation to characterize the onset of contact with an obstacle. This minimum coordinate representation is analyzed to identify active contact constraints through solution of a linear complementarity problem. Knowledge of the active constraints will allow us to define the admissible motion subspace that describes the motions of the vehicle that are admissible with the ground and obstacle contacts.

4.1 Dynamic Model

The dynamic model of the vehicle is built using rigid bodies connected by selecting a minimum coordinate representation with respect to the joints. This way we obtain a n degree of freedom model representing the motion of the chassis and the relative motion of the suspension elements and the wheels, where n sums the rigid body modes of motion of

the overall vehicle and the unconstrained joint movements. If each joint is locked then 6 degrees of freedom will remain. In the case of a vehicle in contact with the environment, $\boldsymbol{\lambda}_w$ contains the set of wheel-ground contact forces, normal and friction, transformed into the chosen set of generalized velocities by the constraint Jacobian \mathbf{A}_w^T . We can then write

$$\mathbf{M}\dot{\mathbf{v}} + \mathbf{c}(\mathbf{v}, \mathbf{q}) = \mathbf{A}_w^T \boldsymbol{\lambda}_w + \mathbf{f}_o \quad (4.1)$$

where \mathbf{M} is the generalized mass matrix, \mathbf{c} includes the nonlinear inertial terms, \mathbf{v} contains the generalized velocities of the vehicle and \mathbf{q} contains the system coordinates. The remaining generalized forces, such as gravitational and actuator forces are collected in \mathbf{f}_o .

4.2 Impulse-Momentum Formulation

Analysis of an impact problem is best done at the impulse-momentum level. Reformulating Eq. (4.1) as an impulse-momentum problem can begin with the definition of generalized momentum \mathbf{p} using kinetic energy T

$$\frac{\partial T}{\partial \mathbf{v}} = \mathbf{p} = \mathbf{M}\mathbf{v} \quad (4.2)$$

and combines $\dot{\mathbf{p}}$ with Eq. (4.1) to yield

$$\dot{\mathbf{p}} - \dot{\mathbf{M}}\mathbf{v} + \mathbf{c} = \mathbf{A}_w^T \boldsymbol{\lambda}_w + \mathbf{f}_o \quad (4.3)$$

Consider Eq. (4.3) over a very short time interval $[t_1, t_2]$, with t_1 just before the onset of contact with an obstacle and t_2 just after. This is shown for a wheel contacting a slope in Fig. 4.1 with an exaggerated scale. Over such a time interval the change in system

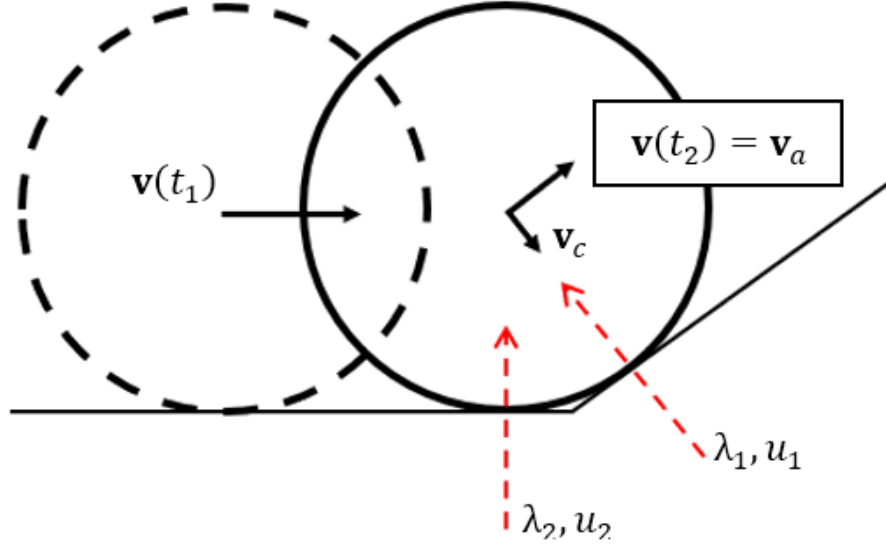


Figure 4.1: Wheel immediately before and after onset of contact

configuration will be minimal. Therefore \mathbf{A}_w can be considered constant, and it may be assumed that $\dot{\mathbf{M}} \approx 0$ [17]. With this approximation, the impulse-momentum level equations can be obtained from Eq.(4.3) for time interval $[t_1, t_2]$ as

$$\mathbf{p}_2 - \mathbf{p}_1 + \bar{\mathbf{c}} = \mathbf{A}_w^T \bar{\boldsymbol{\lambda}}_w + \bar{\mathbf{f}}_o \quad (4.4)$$

where $\bar{\mathbf{c}} = \int_{t_1}^{t_2} \mathbf{c} dt$, $\bar{\boldsymbol{\lambda}}_w = \int_{t_1}^{t_2} \boldsymbol{\lambda}_w dt$ and $\bar{\mathbf{f}}_o = \int_{t_1}^{t_2} \mathbf{f}_o dt$ represent the the impulses of the different generalized forces. The impulsive effect of the nonlinear inertial forces, actuator efforts and gravity forces over this short period of time is predicted to be significantly lower when compared to the contact and inertial forces, and so can be neglected [25]. For the same reason, the segment of $\mathbf{A}_w^T \bar{\boldsymbol{\lambda}}_w$ relating to friction is eliminated. Considering these

assumptions, Eq. (4.4) can be rewritten as

$$\mathbf{M}(\mathbf{v}(t_2) - \mathbf{v}(t_1)) = \mathbf{A}_w^T \bar{\boldsymbol{\lambda}}_w \quad (4.5)$$

which describes how the momentum of the system reacts to impulses caused by the contact forces that arise during the onset of contact with an obstacle.

4.3 Determination of Active Constraints

The constraint Jacobian \mathbf{A}_w represents the modes of motion constrained by the wheel-ground interaction. A natural choice for the wheel constraint directions are the normal directions to the ground at each contact point. \mathbf{u}_w collects the velocities along these directions. Examples for these directions are shown in red in Fig. 4.1. Discretizing the constraint relationship $\mathbf{A}_w \mathbf{v} = \mathbf{u}_w$ across the time interval $[t_2, t_1]$ results in

$$\mathbf{A}_w \Delta \mathbf{v} = \Delta \mathbf{u}_w \quad (4.6)$$

where $\Delta \mathbf{v} = \mathbf{v}(t_2) - \mathbf{v}(t_1)$ and $\Delta \mathbf{u}_w = \mathbf{u}_w(t_2) - \mathbf{u}_w(t_1)$. Combining this equation with Eq. (4.5) yields

$$\mathbf{A}_w \mathbf{M}^{-1} \mathbf{A}_w^T \bar{\boldsymbol{\lambda}}_w = \Delta \mathbf{u}_w \quad (4.7)$$

which relates the contact impulses $\bar{\boldsymbol{\lambda}}_w$ to the velocity jump $\Delta \mathbf{u}_w$ along contact normals at each point.

With the addition of further information about the nature of the contact forces, the contacts that exert an impulse during the onset of contact with an obstacle can be determined. Normal terrain does not adhere to vehicle wheels, so the normal impulse at

any contact point cannot be negative. Additionally, the wheel cannot penetrate the ground. Finally, no impulse can be exerted at a given point unless the wheel and ground remain in contact at that point and vice-versa. These three conditions can be expressed as inequality constraints and complementarity conditions as

$$\mathbf{0} \leq \Delta \mathbf{u}_w \perp \bar{\boldsymbol{\lambda}}_w \geq \mathbf{0} \quad (4.8)$$

which in combination with Eq. (4.7) describes a linear complementarity problem (LCP).

In case of a four-wheeled vehicle contacting a slope, six possible contact points need to be considered: two for each front wheel contacting the slope, two for each front wheel contacting the ground (both shown in Fig. 4.1) and two for each rear wheel contacting the ground. The wheel-slope contact points are not subject to the complementarity conditions, as the onset of contact means they must both exert an impulse and have a velocity jump $\Delta u_1 = u_1(t_2) - u_1(t_1)$ along the direction shown in Fig. 4.1. The exact value of the velocity jump can be determined by projecting $v(t_1)$ along the obstacle normal direction. This velocity jump is an input on the right hand side of Eq. (4.7), as the wheel is not in contact with the slope at t_1 . Therefore, a negative velocity does not require penetration of hard ground, and a velocity change does not mean that the wheel is leaving contact and cannot transmit contact force. Solving the LCP directly without this additional input information would result in a trivial solution of the complementarity problem.

The impulses of the remaining contact points can be determined by the solution of the resulting LCP, for example, by direct pivoting methods [17]. A unique solution for this LCP will exist if the lead matrix $\mathbf{A}_w \mathbf{M}^{-1} \mathbf{A}_w^T$ is a P-matrix, i.e. all principal minors are positive [26, 27]. In general, depending on the number of contacts and their dependence among them, $\mathbf{A}_w \mathbf{M}^{-1} \mathbf{A}_w^T$ may be singular and therefore the LCP will not be solvable, as a

singular matrix will contain non-positive principal minors. In the studied example, this is indeed the case, and the full set of 6 contact points describe a linearly dependant relationship between $\bar{\boldsymbol{\lambda}}_w$ and $\Delta \mathbf{u}_w$. One possible physically meaningful solution is to use a projection employing a weighted generalized inverse to solve for $\boldsymbol{\lambda}_w$, with a weighting matrix that describes the relationship between the stiffness at each contact [28]. In this study, equal stiffness between wheels was assumed, so no weighting matrix is required. Additionally, the exact value of each impulse is not required, so exact stiffness values are unnecessary.

Once $\bar{\boldsymbol{\lambda}}_w$ is calculated, the active subset of wheel-terrain constraints is represented by the rows of \mathbf{A}_w that correspond to a positive impulse, and therefore carry load during the onset of contact. These rows are associated with the active contacts and collected in matrix \mathbf{A}_{act} .

4.4 Admissible Velocity Calculation

With a complete list of active constraints represented by \mathbf{A}_{act} , the velocities describing the motion of the vehicle can be decomposed into the constrained subspace of motion defined by $\mathbf{A}_{act} \mathbf{v} = \mathbf{u}_c$, and the orthogonal admissible subspace of motion unaffected by the constraints [29]. This decomposition can be performed by assembling the projector matrices

$$\mathbf{P}_c = \mathbf{M}^{-1} \mathbf{A}_{act}^T \left(\mathbf{A}_{act} \mathbf{M}^{-1} \mathbf{A}_{act}^T \right)^{-1} \mathbf{A}_{act} \quad (4.9)$$

$$\mathbf{P}_a = \mathbf{I} - \mathbf{P}_c \quad (4.10)$$

which can be used to produce a mass-orthogonal decoupling and decompose the generalized velocities to admissible velocities $\mathbf{v}_a = \mathbf{P}_a \mathbf{v}$ and constrained velocities $\mathbf{v}_c = \mathbf{P}_c \mathbf{v}$. This projection into mass-orthogonal sub-spaces by definition results in a full decomposition of constrained and admissible velocities with no coupling terms remaining.

4.4.1 Selected Performance Indicators

The projections mentioned above can be used to decouple the kinetic energy as

$$T = T_a + T_c = \frac{1}{2} \mathbf{v}_a^T \mathbf{M} \mathbf{v}_a + \frac{1}{2} \mathbf{v}_c^T \mathbf{M} \mathbf{v}_c \quad (4.11)$$

where, at a given moment, T_a is the kinetic energy associated with the admissible motion and T_c is the kinetic energy associated with the constrained motion. T_a and T_c can also be referred to as admissible and constrained kinetic energy, respectively. The above relationship is valid at any instant along the trajectory, but is only expected to be useful in predicting obstacle negotiation performance when evaluated immediately before impact. Therefore, T_a will be used in the rest of this work to refer to the value calculated in the pre-impact instant.

During the compression phase of the contact onset with the obstacle all constrained kinetic energy is absorbed. As the wheel remains in contact with the obstacle, we can assume that the related coefficient of restitution is zero, and the pre-impact T_c will not be recovered. The assumption of zero coefficient of restitution is shown to be valid especially in relatively high speed impacts [25]. The value of T_a calculated pre-impact should then measure all kinetic energy remaining after impact to aid in negotiating an obstacle [17]. However, T_a quantifies all kinetic energy not effected by the unilateral and bilateral constraints, which may contain modes of motion that are not used in climbing the obstacle. Therefore, a related indicator named T_{a-COM} is developed. This indicator first extracts the admissible velocity corresponding to the main body from \mathbf{v}_a . This velocity is then decomposed in some chosen coordinate system at the vehicle's center of mass, and projected along the direction of the obstacle as shown in Fig. 4.2. This results in a scalar speed v_{ao-COM} that represents the admissible velocity along the intended trajectory. Combining this with the total mass m of the vehicle allows calculation of this performance indicator as

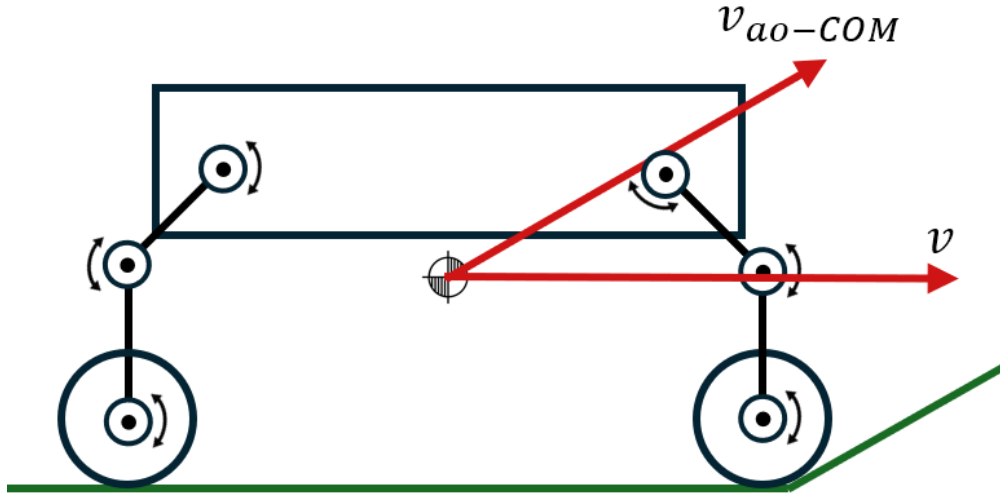


Figure 4.2: v and v_{ao-COM} on a 2d representation of an actively actuated vehicle

$$T_{a-COM} = \frac{1}{2}mv_{ao-COM}^2 \quad (4.12)$$

A third possible performance indicator can be defined as the unlocked admissible kinetic energy, or T_{a-ul} . This performance indicator captures the admissible kinetic energy of the vehicle if the joints are unactuated at the onset of contact and are therefore able to move. T_{a-ul} is calculated in the same way as T_a , except the joint lock constraints are not included in the Jacobian of active constraints A_{act} . A situation in which the joints are fully unlocked is unlikely, as the robot would be unable to maintain its configuration. However, this calculation may be more representative of a situation where there is a significant amount of slack or flexibility, or both, in the actuated joints, and therefore joints rotate a finite amount at the onset of contact.

4.5 Energy Analysis of Obstacle Negotiation

It has been hypothesized that since T_a predicts the kinetic energy conserved after initial contact, it can be directly compared to the gravitational potential energy required to reach the top of an obstacle [13]. A more detailed energy analysis outlines the other factors at play. Consider a system made up of a vehicle of mass m travelling at speed v towards an obstacle with angle θ . At time t_1 , immediately before contact it will have some kinetic energy T_1 . At time t_2 immediately after the onset of contact, it will have kinetic energy $T_2 = T_a(v, q, \theta)$ as discussed previously. Using conservation of energy $W_{net} = \Delta T + \Delta U$, the definition of work with constraint forces $\boldsymbol{\lambda}_c$ and displacements \mathbf{u}_c , and Eq. (4.11)

$$W_{net} = W_c = -T_c = \int_{t_1}^{t_2} \boldsymbol{\lambda}_c \cdot \mathbf{u}_c dt \quad (4.13)$$

The assumption of no configuration change means $\Delta U = 0$ and the only work done on the system is by the constraint forces written as W_c .

Consider then a time t_3 , where the robot has reached its maximum height on the sloped obstacle and its speed is 0: either because the maneuver and therefore the drive motors are stopped or because the combination of momentum and wheel friction are insufficient to continue. This state can be compared to t_2 using conservation of energy, where the change in potential and kinetic energies are written as $\Delta U = mg\Delta h$ and $\Delta T = 0 - T_a$. The net work W_{net} is a combination of the work done on the vehicle through friction by the wheels W_f , and the other constraint forces between the wheels and terrain W_c . The wheel work can be measured directly through a combination of current sensors and knowledge of the torque constant of the drive motors. W_f will be positive as the drive motors use friction to create force in the direction of motion, and W_c will be negative as the terrain's contact normals oppose the direction of motion. Conservation of energy between t_2 and t_3 can then

be written as

$$T_a + W_f + W_c = mg\Delta h \quad (4.14)$$

W_c is a quantity that is difficult to calculate directly, as it requires forward dynamics simulation to either calculate λ_c throughout the maneuver, or recalculate T_c based on $\mathbf{v} = \mathbf{v}_a$ from the previous time step. However, based on Eq. (4.11) increasing T_a must necessarily decrease T_c and therefore W_c . Additionally, as will be shown based on later experimental results, the configuration of a given vehicle that optimizes T_a does not depend strongly on obstacle angle, even though T_a itself does. Therefore, increasing T_a at the onset of contact should improve obstacle negotiation ability represented by Δh even as the obstacle angle relative to the vehicle changes throughout the maneuver. T_a cannot be directly compared to the height of an obstacle, but it may still be a useful performance indicator as will be demonstrated empirically in the following section.

Chapter 5

Results

A set of robot joint configurations for obstacle negotiation testing were determined. All testing is performed for negotiation of a slope with an angle of between 20° and 40° . The solution of the LCP is validated in the robot's neutral configuration. Then, the impact of the selected performance indicators on obstacle negotiation is assessed through analysis of negotiation maneuvers using the set of joint configurations developed in the following section.

5.1 Configuration Optimization

The value of selected performance indicators for a given vehicle depend on its configuration and the obstacle slope. To isolate the effect of T_a and T_{a-COM} , tests must be performed at different configurations. An optimization process was performed to identify the configurations (or joint positions \mathbf{q}) with the highest and lowest T_a , to create as large a variation between low and high T_a maneuvers as possible. As is common to obstacle negotiation maneuvers, stability, traction and collision avoidance need to be considered. The effect of traction was not considered explicitly in this optimization process, as it is

dependent on contact weight distribution and therefore difficult to separate from T_a and T_{a-COM} . Additionally, the current sensors allow the torque exerted by the motors to be recorded and therefore the effect of tractive forces to be removed from the analysis.

T_a is optimized directly, subject to stability and obstacle avoidance constraints. Maintaining stability ensures that any loss of wheel contact is due to the impact as predicted through solution of the LCP. Stability is maintained by constraining the robot COM between the front and rear wheel contact points, both on the flat ground and on the angle obstacle. Collision avoidance considers the relative positions between the robot joints and the terrain to prevent any unintended contacts. Finally, the list of joint positions \mathbf{q} was subject to joint limits.

This problem was solved using MATLAB's `fmincon` function, using sequential quadratic programming, with a constraint tolerance of 10^{-6} . The resulting configurations are shown below in Fig. 5.2, with maximum and minimum predicted T_a respectively. The joint angles $\mathbf{q} = [\text{RE RS FS FE}]$ are listed as angles relative to the previous link or main body in order of: rear elbow (RE), rear shoulder (RS), front shoulder (FS) and front elbow (FE), see Fig. 5.3. Left and right suspension sets are kept symmetric. This optimization was performed for the full set of possible obstacle angles. However, this set of optimization solutions produced only minimally different configurations, likely to satisfy the stability and collision constraints at each angle, with the obstacle angle not otherwise affecting the optimal configuration. Therefore, the results optimized for 40° are used for experiments at every angle.

Finally, a third neutral configuration is chosen that holds the main body flat and has a wide enough stance to remain stable at all tested angles. This serves as a base case for a feasible but unoptimized point of comparison.

Configuration Name	Joint Angles ($^{\circ}$)	T_a at 25° (J)	T_a at 35° (J)
Default	[45 45 -45 -45]	3.64	3.06
Maximized T_a	[85 70 -16 7.7]	3.84	3.49
Minimized T_a	[20.5 72 -72 -62]	3.39	2.76

Table 5.1: Summary of generated configurations

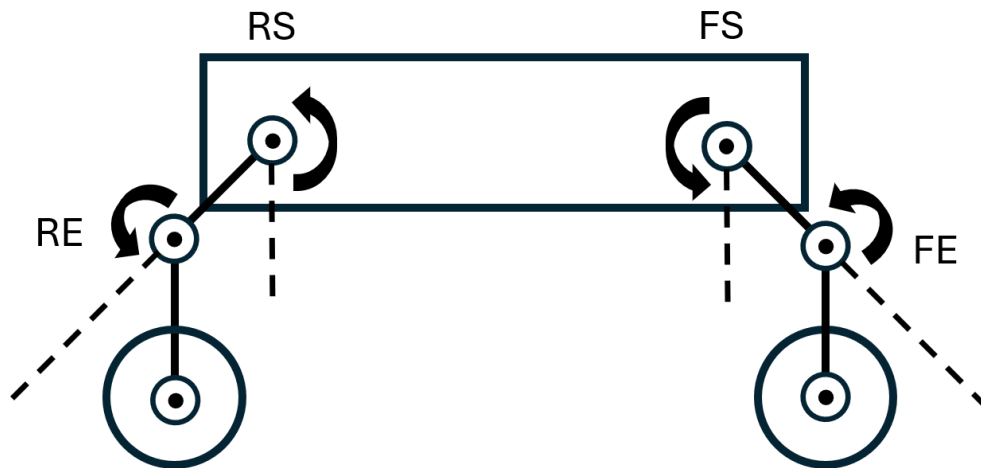


Figure 5.1: Diagram of robot with joint labels and origin lines

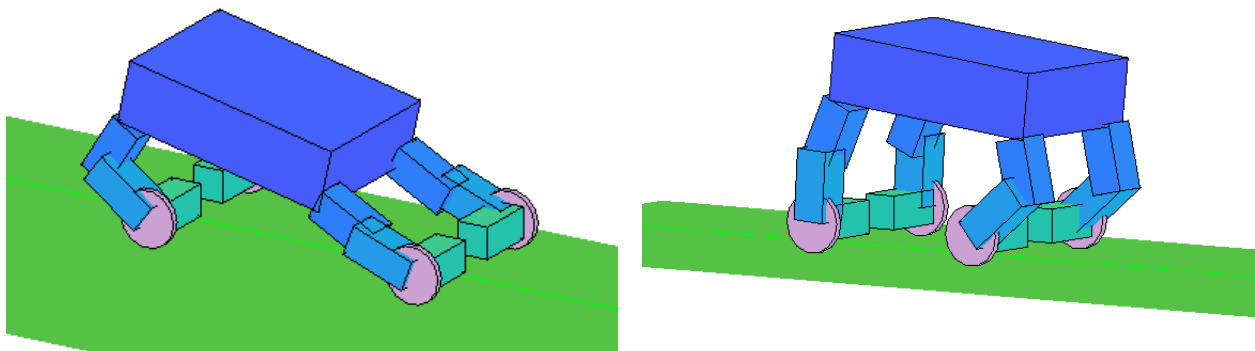


Figure 5.2: a) High T_a configuration, b) low T_a configuration

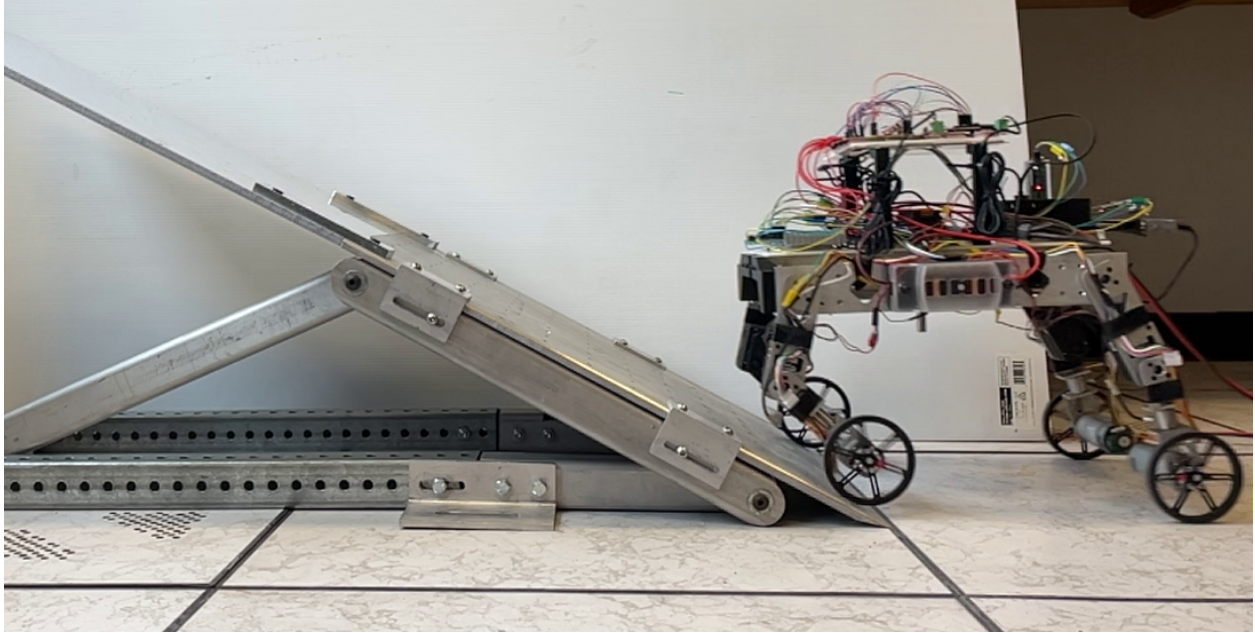


Figure 5.3: Robot in low admissible configuration contacting an obstacle

5.2 Active Contact Prediction

The solution of the LCP must be verified to ensure that the selection of active contacts for calculation of selected performance indicators is correct. Experimental confirmation of active contact prediction will also provide evidence of the accuracy of the dynamic model used. Inactive contacts generally correspond to a velocity jump and separation at the contact point and can therefore be confirmed visually.

The LCP was solved for the robot in neutral configuration negotiating a slope at angles from 20° to 40° at an initial approach speed of $1.13 \frac{m}{s}$. This experimental setup is shown in Fig. 5.3. Robot configuration was measured through encoder based joint angle reading and obstacle angle was verified using a level. At the tested range of obstacle angles, the contact between the front wheels and the ground is always inactive, and the contact between the front wheels and the obstacle is always active. The rear wheel-ground contacts are predicted

to be active at an obstacle angle below 27.2° and inactive otherwise. A set of maneuvers were filmed to confirm this result.

The front wheel-ground contact being inactive indicates that the robot will tend to travel up the obstacle after contact. Front wheel-ground and wheel-obstacle contacts being active at the same time would indicate that the robot tips forward at the onset of contact without advancing up the slope. Any admissible kinetic energy calculated at this angle would measure this tipping mode of motion that does not aid in obstacle negotiation. In the neutral configuration, both front wheel contacts are active at obstacle angles of 70° and higher. This angle corresponds to the point at which admissible kinetic energy reaches its non-zero minimum, which previous work has also predicted indicates the inflection point of a tendency to climb the obstacle [17]. This result is not confirmed experimentally, as it is not the main focus of this work and the high obstacle angle increases the likelihood and damage of unintentional collisions.

A preliminary set of filming was conducted with a 720p camera filming at 240fps. This was unable to detect any contact loss at the rear wheel regardless of obstacle angle. Therefore, a further set of experiments were performed using a high speed camera, the Photron SA-5. Two videos were captured at each obstacle angle [23° , 25° , 30° , 35° , 40°] at 5000 fps with an exposure time of $1/15000$ s, and a resolution of 1024×1024 . Object tracking of the wheel center through video analysis was then performed using Kinovea, an object tracking software. This wheel center trajectory is shown in orange and red in Fig. 5.4 and Fig. 5.5 respectively.

Figure 5.4. shows that contact with an obstacle angle of 30° produced a velocity jump, with a visible vertical displacement of 2mm over 40ms at 30° . Contact with an obstacle of 25° , shown in Fig. 5.5. produces some vibrations within the object tracking accuracy of ± 0.75 mm but does not appear to lose contact. This was confirmed by inspection of the wheel-ground contact area during impact. The dynamic model of the robotic test platform

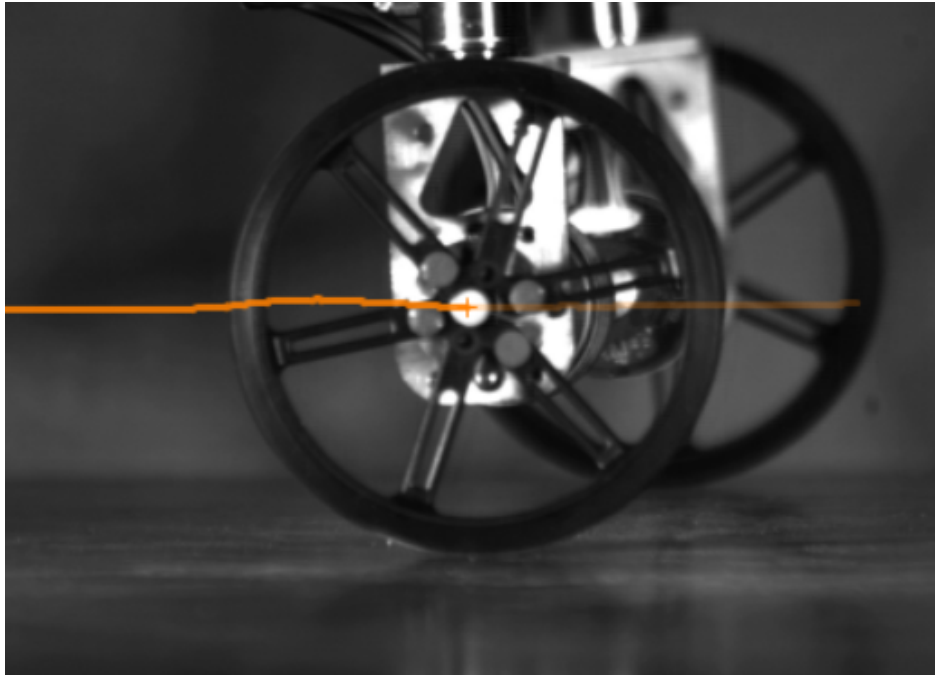


Figure 5.4: Analysis of contact with 30° obstacle

assumes that all the joints are locked on impact and perfectly rigid. As the robot's joints are stabilized by servomotor actuators and not mechanical locks, they may add some additional flexibility to the system. In combination with thin rubber tires this may cause the wheel center to move slightly in response to the loads sustained under impact even as the wheel edge maintains contact with the ground. Analysis of experiments at obstacle angles of 35° and 40° show the rear wheel losing contact as predicted. Combined with results from 25° and 30°, this validates the selection of active contacts for use in admissible velocity calculation in subsequent experiments. Additionally, evidence in support of a transitional obstacle angle of 27.2° is obtained, as the rear wheel maintains contact at 25° and lifts at 30°. Experiments at angles closer to the transition angle are not attempted, as the predicted displacement is too low to distinguish from an active contact with the precision of the current method.

A close up video was taken of the front wheel as it contacts a 40° obstacle. Comparing

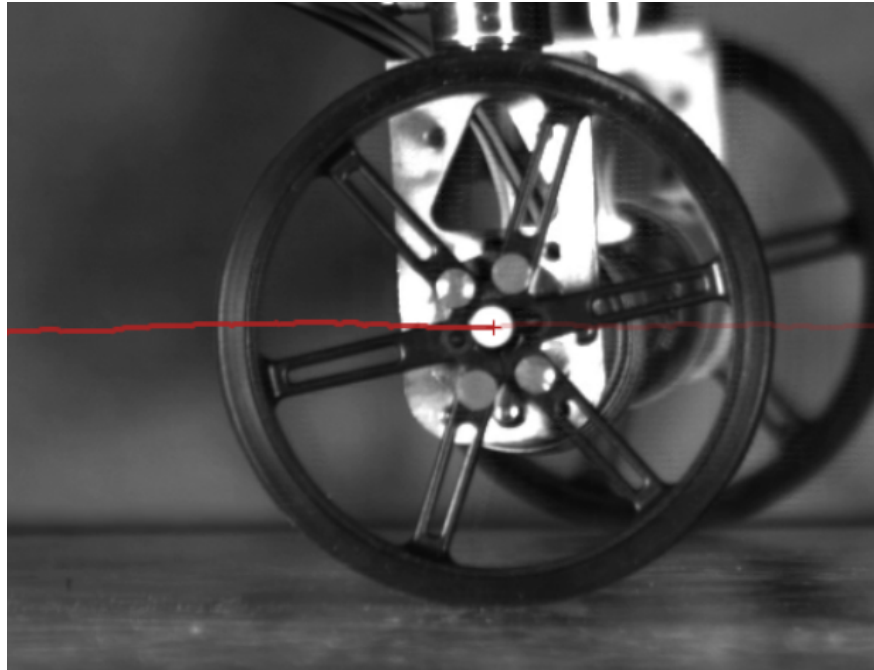


Figure 5.5: Analysis of contact with 25° obstacle

the moment at which the wheel begins to contact the obstacle to when a slight rebound motion begins yields a contact duration of approximately 11ms. At this contact duration, the impulse from gravity would be approximately 0.18 Ns per wheel. By comparison, the impulse calculated from the LCP per wheel in contact is 2.13 Ns . At 8% of the value of the calculated impulse, including the effect of gravity may slightly improve the accuracy of the linear complementarity problem solution. However, the previous results show that Eq.4.5 is still highly representative of the contact dynamics to the precision detectable by the current experimental setup.

5.3 Motion Analysis Experiments

5.3.1 Motion Analysis Setup

The pre-impact value of the admissible kinetic energy, T_a , can be used as a measure to predict the total kinetic energy of the robot at the instant after impact. As the admissible kinetic energy is a continuous function of time $T_a(t)$, it can hold different values depending on the instant during the trajectory that it is calculated. In this section, T_a refers to the value calculated immediately before the onset of contact, using the pre-impact velocity and the ground and slope constraints corresponding to the solution of the LCP. To attempt to validate this calculation directly, the velocity of the robot must be measured instantaneously as the front wheel contacts the obstacle. Velocity is difficult to measure directly. Drive wheel encoders can be used but the possibility of slip between wheel and terrain introduces too much uncertainty. Readings from the IMU, such as gyroscope derived angular velocities and accelerometer measurements can be combined and integrated to measure speed. These readings are generally very noisy, and limited to 200Hz by the data collection system, and therefore this option was discarded. Velocity measurement through high-speed camera filming was chosen instead, as this allows velocity to be calculated directly with a higher measurement speed than that of the IMU.

The Photron SA-5 was used for this high-speed filming. Three videos per configuration were captured at each obstacle angle $[25^\circ, 30^\circ, 35^\circ]$ at 5000 fps with a shutter speed of $1/15000$ s, and a resolution of 1024×1024 . Reflective motion tracking stickers were added to each wheel center and the main body. The camera is set up to capture the full profile of the mobile robot for 100ms before and after the onset of contact between the front wheel and the obstacle. This setup is shown in Fig. 5.6.

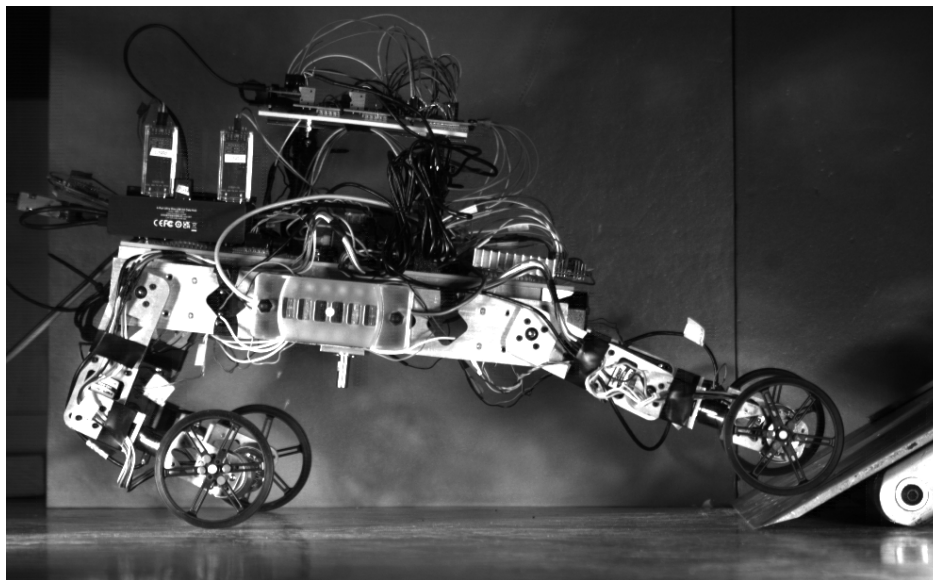


Figure 5.6: Photron capture setup

5.3.2 Motion Analysis

Post-processing of the high speed camera footage is performed using Kinovea to capture the displacement and velocity of the front and back wheels, and main body centre. Recorded velocity measurements are passed through a Kalman filter to reduce noise. Length calibration is performed using the known internal wheel diameter of 67.75mm.

Calculation of kinetic energy for a rigid body is performed as below:

$$T = \frac{1}{2}m\mathbf{v}_B \cdot \mathbf{v}_B + \frac{1}{2}\boldsymbol{\omega} \cdot \mathbf{I} \cdot \boldsymbol{\omega} + m\mathbf{v}_B \cdot (\boldsymbol{\omega} \times \boldsymbol{\rho}_{BG}) \quad (5.1)$$

where B is any point that moves with the vehicle and G is the position of the centre of mass. v_B is measured directly from the main body point tracking, and the angular velocity $\boldsymbol{\omega}$ is derived by comparing the velocity of the three tracked points. The position of the centre of mass relative to the middle tracked point $\boldsymbol{\rho}_{BG}$ and the moment of inertia \mathbf{I} are configuration dependant, and so are recalculated for each experiment depending on the recorded joint

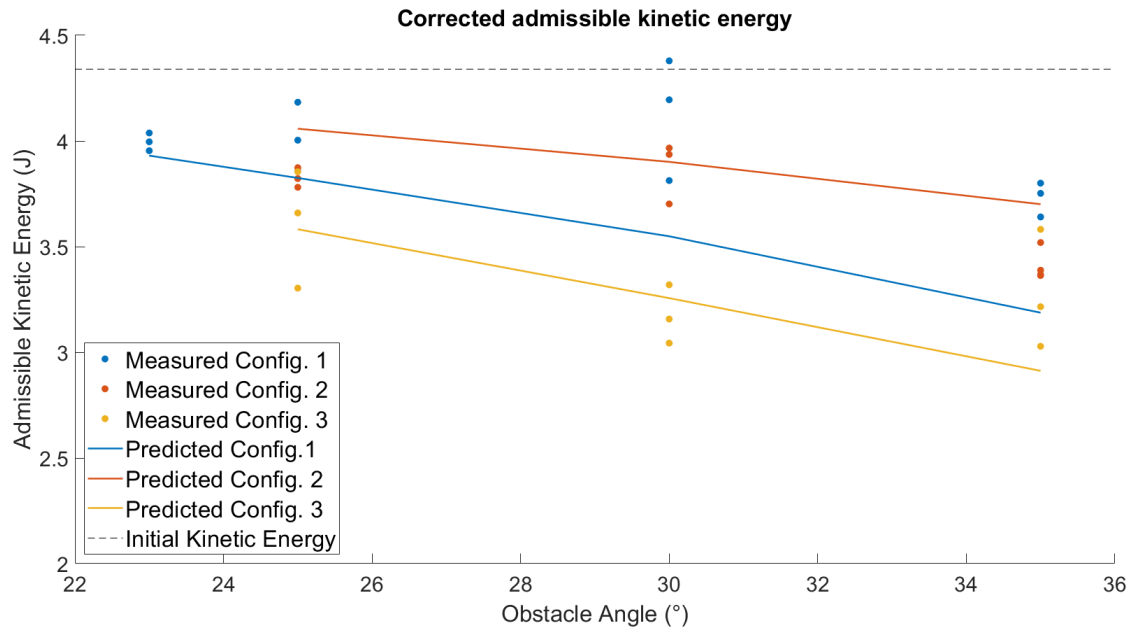


Figure 5.7: Summary of corrected kinetic energy

positions.

According to a rigid body model and inelastic obstacle model contact, the velocity should change near instantaneously after the onset of contact. However, inspection of the velocity trajectories show that change is more gradual, with a near linear increase of angular velocity for 15-40ms after the onset of contact. Therefore, to achieve as clear a comparison between configurations as possible all kinetic energies are calculated at the peak vertical velocity of the front wheel. This delay, however, means that other impulses will become significant, such as the effect of gravity and wheel torques. Using current sensor measurements and COM displacement, these energies are compensated for, leaving only the admissible kinetic energy.

A summary of these results are shown in Fig.5.7, with experimental data points plotted alongside solid lines representing the expected kinetic energy. Though average error is a

moderate 8.7%, the graphical representation of the results show clearly that strong conclusions cannot be drawn from these results. Certain experiments show a high degree of agreement with prediction, such as the neutral configuration at 23°, the low admissible configuration at 25° and 30° and the high admissible configuration at 30°. However, the neutral configuration has a consistently higher kinetic energy than the optimized configuration, to the point of measuring higher kinetic energy than before the collision in one experiment. Additionally, each configuration has at least one experiment where increasing obstacle angle increases kinetic energy, instead of decreasing it, which contradicts all calculations as well as previous work. Other possible measures of admissible kinetic energy such as T_{a-ul} and T_{a-COM} have slightly higher errors: 12.55% and 17.4% respectively. None show a significant correlation with measured T_a , indicating that the discrepancy is not just the result of a systematic error.

These discrepancies may be explained by a combination of theoretical simulation assumptions and limitations of the measurement system. In Eq. 4.5 we are able to assume that all constrained kinetic energy is dissipated during contact with the obstacle by setting the time t_2 at the end of the compression phase of impact, or by assuming that the coefficient of restitution is 0, and therefore the restitution phase of impact does not change the vehicle's energy. As the energy analysis is performed some 15-40ms after the onset of contact, the kinetic energy may incorporate some energy from rebound that was assumed to be negligible, and which may also be configuration and obstacle angle dependant. Additionally, the flexibility of the joints is assumed to be negligible in the momentum analysis. Joint motion may be present and as the joint actuator current is not measured cannot be compensated for. This movement will also be configuration and obstacle angle dependant and therefore another significant component of the unexpected results.

At time scales on the order of 15-40ms, measurement precision may also lead to increased

error. The current sensors have a measurement rate of 180Hz, which means that only around 3-8 measurements lie within the relevant time-frame for each experiment. Measurement noise may then be a significant factor. Additionally, the tracking markings with a 6mm diameter are about 12px wide, leaving a maximum precision of $\pm 0.25\text{mm}$, before the accuracy of the object tracking itself is considered. Investigation of the object tracking shows oscillation of $\pm 0.75\text{mm}$ from what should be a flat trajectory. Velocity measurements are averaged and filtered across multiple frames, but this displacement precision can have large effects on the potential energy calculations of about %15.

Overall, these sources of error combined with the inconclusive results do not support the prediction of admissible kinetic energy. Additional experiments will need to be performed over a full obstacle negotiation maneuver to attempt to reduce the effect of measurement noise as well as the impact of factors such as the joint flexibility and restitution which will be most significant at the onset of contact where constraint forces will be highest.

5.4 Full Maneuver Experiments

5.4.1 Experimental Setup

A set of experiments were performed to assess the robot's performance in obstacle negotiation. Five tests were conducted at each of the three configurations determined previously, repeated at obstacle angles of 25° , 30° and 40° . In all experiments the robot had an initial speed of 1.13 m/s corresponding to a wheel angular velocity of 4 rotations/s. This was the highest speed that would ensure the robot stays in the camera field of view throughout the obstacle crossing, while maintaining adequate resolution to reliably track the points marked on the wheel and main body. The robot runs at this speed for 2.2s, with 1m between initial position and obstacle edge to ensure the vehicle can accelerate to its

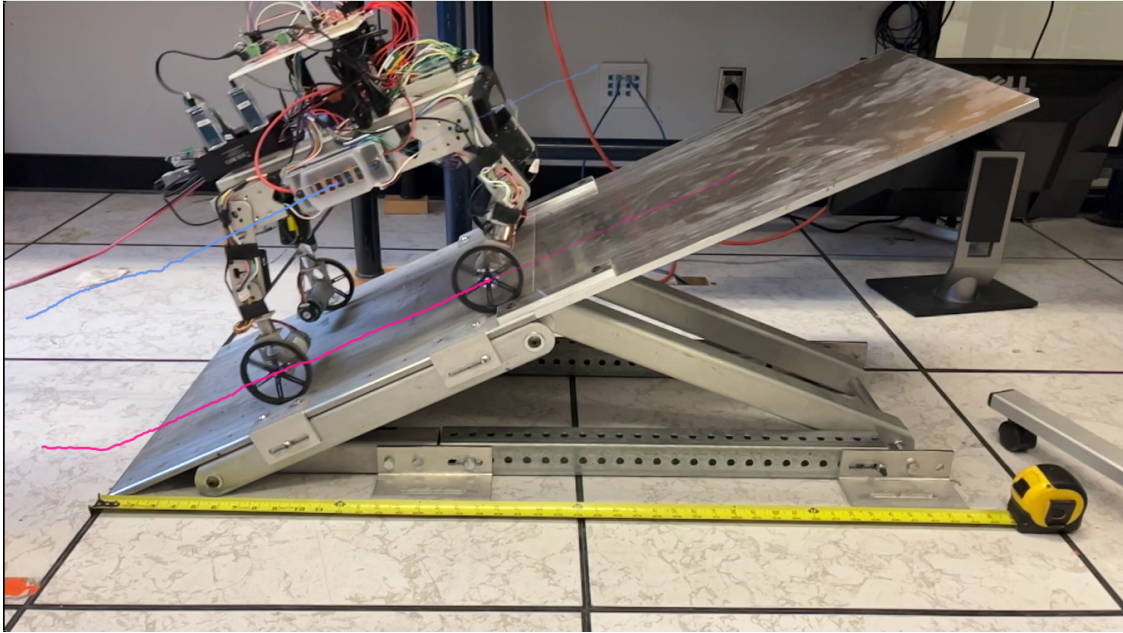


Figure 5.8: Tracking of low T_a configuration

intended speed before the onset of contact. The experimental setup is identical to that used for active contact prediction, shown in Fig. 5.3.

Calculation of T_a and T_{a-COM} are based on initial speed and configuration measurements provided by drive and joint encoders and corroborated by high-speed camera footage. As the entire maneuver lasts 2.2 seconds, and travel distances are on the order of decimeters instead of single millimeters, video footage is captured by a 240 fps camera filming at 720p.

Additional measurements are required to characterize the vehicle's performance based on Eq. 4.14 including the change in height of the vehicle's center of mass Δh and the wheel work W_f done. Δh is measured through tracking of a marked point near to the center of mass of the vehicle, shown in Fig. 5.8. Using the MATLAB simulation, the configuration dependent displacement between the marked point and the actual COM is corrected for to derive Δh . For W_f , the voltage output from the current sensors is converted into current using a sensitivity of 400mV/A. This current is further converted into motor torque by interpolating

between the free and stall operating points provided on the motor datasheet. This assumes that the power losses from gearbox friction and motor inefficiencies are constant. The power $P = Tv$ across the run is calculated in combination with the encoder speed measurements and then summed to yield the total wheel work W_f .

5.4.2 Performance Analysis

The performance indicators T_a , T_{a-COM} and T_{a-ul} , calculated across 45 tests, are plotted against the measure of obstacle negotiation ability, U_g , directly. The potential energy U_g is computed using the vertical displacement of the robot center of mass, between beginning of the manouver and the maximum height attained. Each set of five experiments at a given angle and configuration are merged into one data-point for illustration. A trendline is plotted as a dotted orange line. As shown in Eq. (4.13), the obstacle negotiation performance is also a function of the tractive forces, which are not directly considered in the use of admissible kinetic energy as a performance indicator. To isolate the effect of admissible kinetic energy, the performance indicators are also compared to $U_g - W_f$, where W_f is the total wheel work done.

As can be seen from Fig. (5.9), comparing T_a and U_g alone is not sufficient to characterize the obstacle negotiation ability. T_a only has a mild positive correlation with U_g . However, when U_g is adjusted for the effect of traction the correlation increases to a very strong $R^2 = 0.920$. Considering that the results shown in Fig. 5.9 are obtained over a variety of obstacle angles and configurations, this implies that T_a is predictive of $U_g - W_f$. This result supports the hypothesis that increasing T_a will reduce W_c . Inspection of Eq. (4.14) also explains why $U_g - W_f$ is always calculated to be negative and larger than T_a , as the remaining energy must be primarily dissipated by the constraint forces. A R^2 of 0.920 shows that 8% of the variance of $U_g - W_f$ is not explained by the variance of T_a . This is likely a

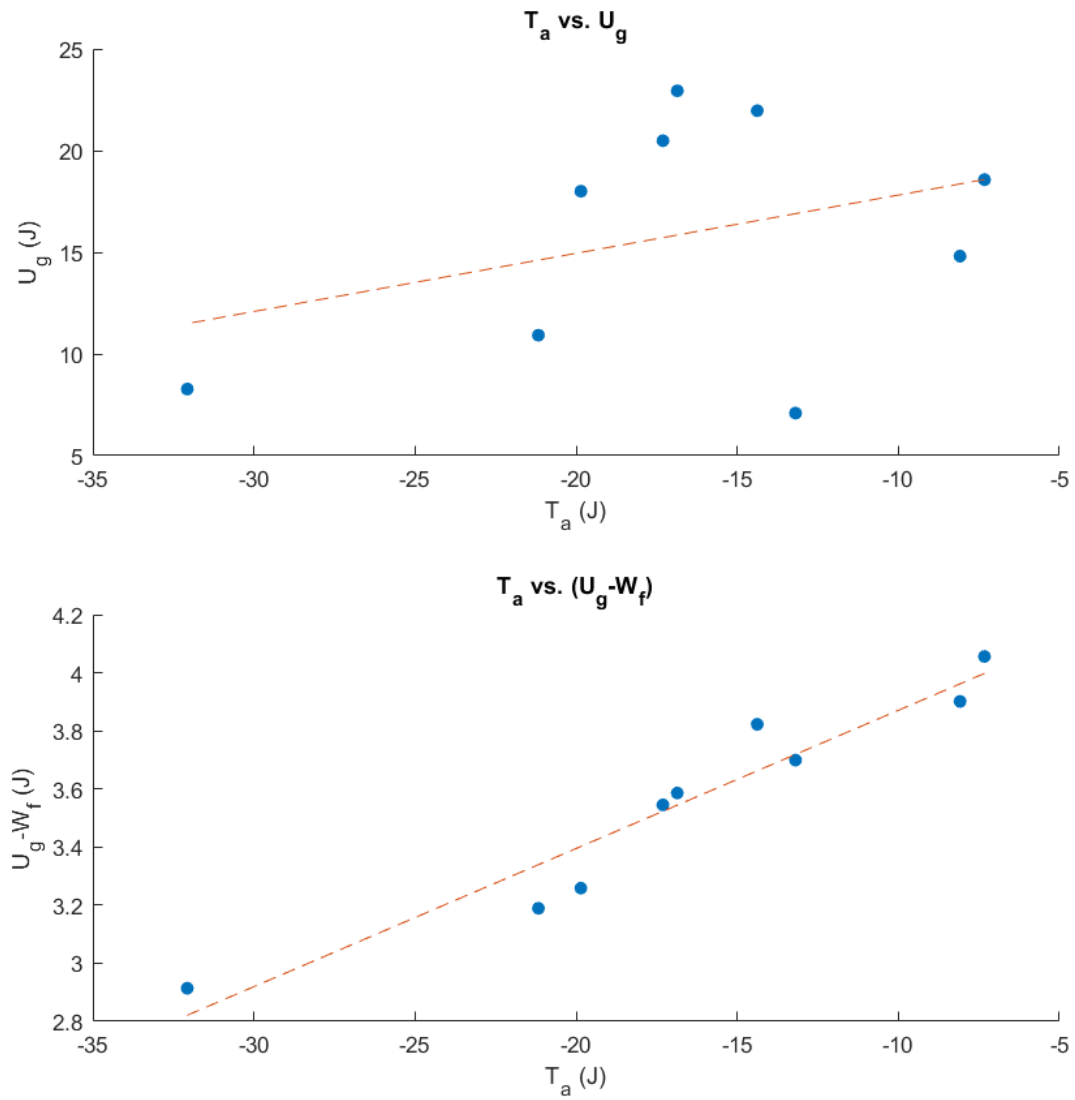


Figure 5.9: T_a as performance indicator without (above) and with (below) traction adjustment

combination of three main factors mentioned throughout this work. First, the actuated joints have some flexibility not incorporated into the locked joint dynamic model that would absorb some additional energy not considered in Eq. (4.14). Second, the coefficient of restitution is assumed to be 0 for calculation of T_a , but is likely some low number that is configuration and obstacle dependent, and may add additional variance into the results. Finally, the dynamic model may not be completely representative of the vehicle, as the exact placement of wires and fasteners were not included in the SOLIDWORKS model used for calculation of the link inertia.

The ability to predict or increase $U_g - W_f$ may not immediately appear useful, as calculating W_f at the planning or design stage requires forwards dynamic simulations that the use of performance indicators attempts to reduce. However, this performance indicator may still be used to alter a robot's configuration to reduce the energy expended to negotiate a given obstacle, which can be useful in situations where energy use or actuator power is constrained. Alternatively, T_a can be used as an optimization goal in conjunction with a performance indicator used for traction to improve the vehicle's performance on a given obstacle.

T_{a-COM} attempts to predict only the admissible kinetic energy that is useful for obstacle negotiation. As it is not calculated based on the kinetic energy decomposition shown in Eq. (4.11), this quantity does not enter directly into the energy analysis in Eq. (4.14) and therefore is not expected to be especially predictive of traction adjusted kinetic energy. As can be seen by comparing these quantities in Fig. 5.10, there is in fact no correlation detected. However, Fig. 5.10 does show a very strong relationship between T_{a-COM} and the measure of negotiated obstacle height U_g . This correlation of $R^2 = 0.921$ is almost identical to that of T_a vs. $(U_g - W_f)$. The high effectiveness of T_{a-COM} as a predictor of obstacle height navigated when traction is not explicitly considered, combined with a near identical

correlation of T_a vs. $(U_g - W_f)$ and T_{a-com} vs. U_g seems to imply that the calculation of T_{a-COM} is implicitly considering some performance indicator for traction as well. This would also explain the complete lack of correlation between T_{a-COM} vs. $(U_g - W_f)$, as if traction is already considered in T_{a-COM} , compensating for it by removing W_f would remove T_{a-COM} 's predictive power.

T_{a-ul} was compared to the same performance metrics as T_a and T_{a-COM} as shown in Fig. 5.11. As can be seen from the resulting correlations, T_{a-ul} is less strongly predictive of obstacle height attained than T_{a-COM} but significantly more predictive than T_a . It is almost completely uncorrelated with traction adjusted height attained. The overall lack of strong predictive power is partially explainable by the lack of current sensing on joint actuators as T_{a-ul} considers possible motion around the joints, but the work done to maintain the joint positions is not measured. It is also possible that T_{a-ul} does capture accurately the motion and energy of the robot at the moment after impact, but the admissible joint motions do not influence later obstacle negotiation ability, explaining the lack of strong correlation with obstacle negotiation metrics.

Overall, both T_a and T_{a-COM} have been demonstrated to be highly predictive of obstacle negotiation performance. T_{a-COM} may appear to be the more useful indicator, as it is directly indicative of the maximum height reached on a slope and requires no adjustment for the effect of traction to optimize a vehicle's performance or predict its obstacle negotiation ability. However, this performance indicator has only been tested on hard terrain, where the main limitation of drive wheel force is the contact normal force controlled primarily by weight distribution. In the case where more advanced techniques, such as traction control or wheel walking are used, or the maximum friction force at the contact points is more complex such as in the case of soft terrain, T_a may be a more useful indicator. Traction can then be handled separately, though further research may show that

T_{a-COM} is an effective performance indicator in more complex circumstances as well. T_a can also be used in situations where reduction of energy lost through terrain interaction is a more critical performance metric than obstacle height negotiated, or where traction is so low or approach speed so high that W_f is considerably less influential than T_a and W_c .

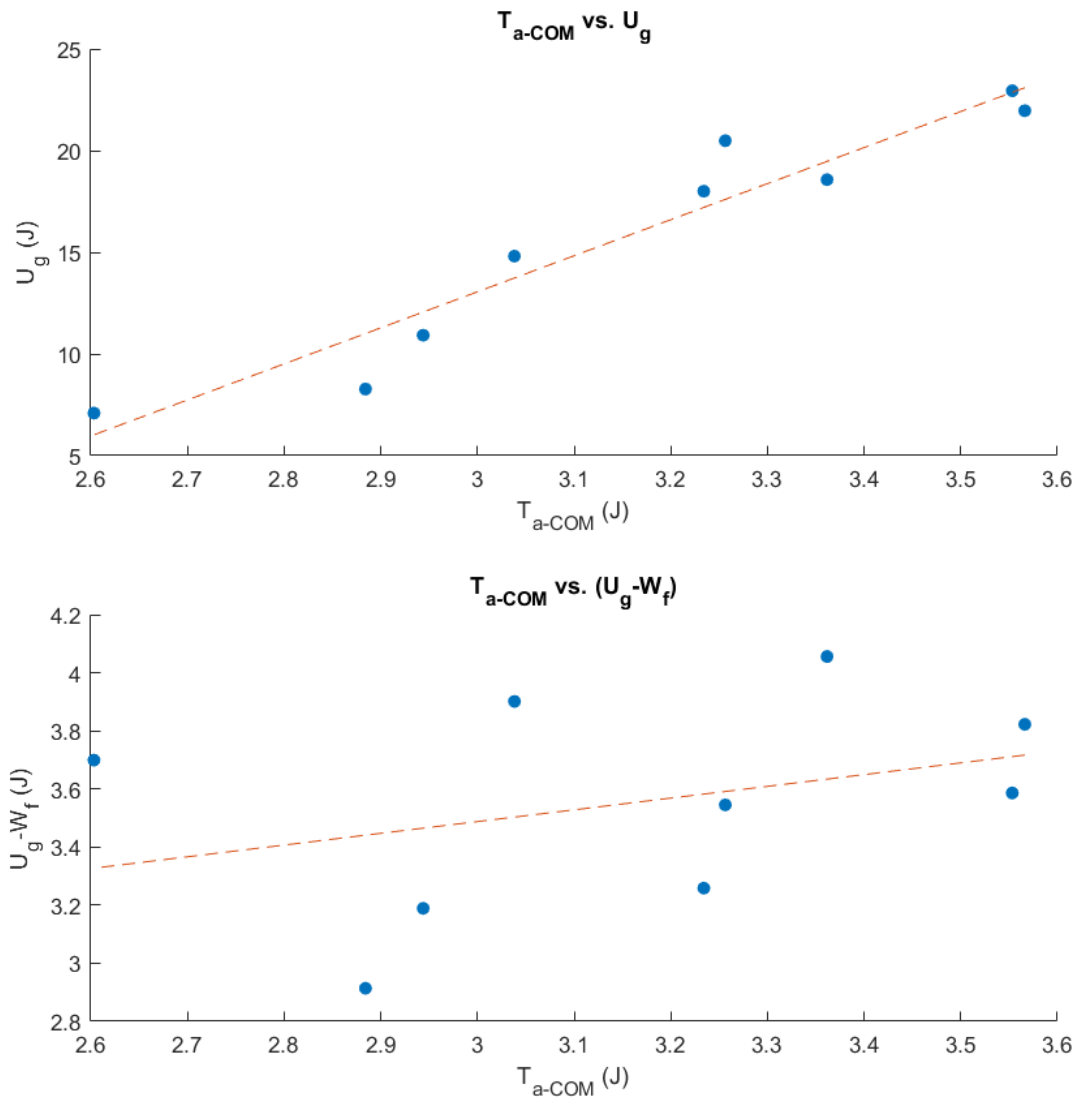


Figure 5.10: T_{a-COM} as performance indicator without (above) and with (below) traction adjustment

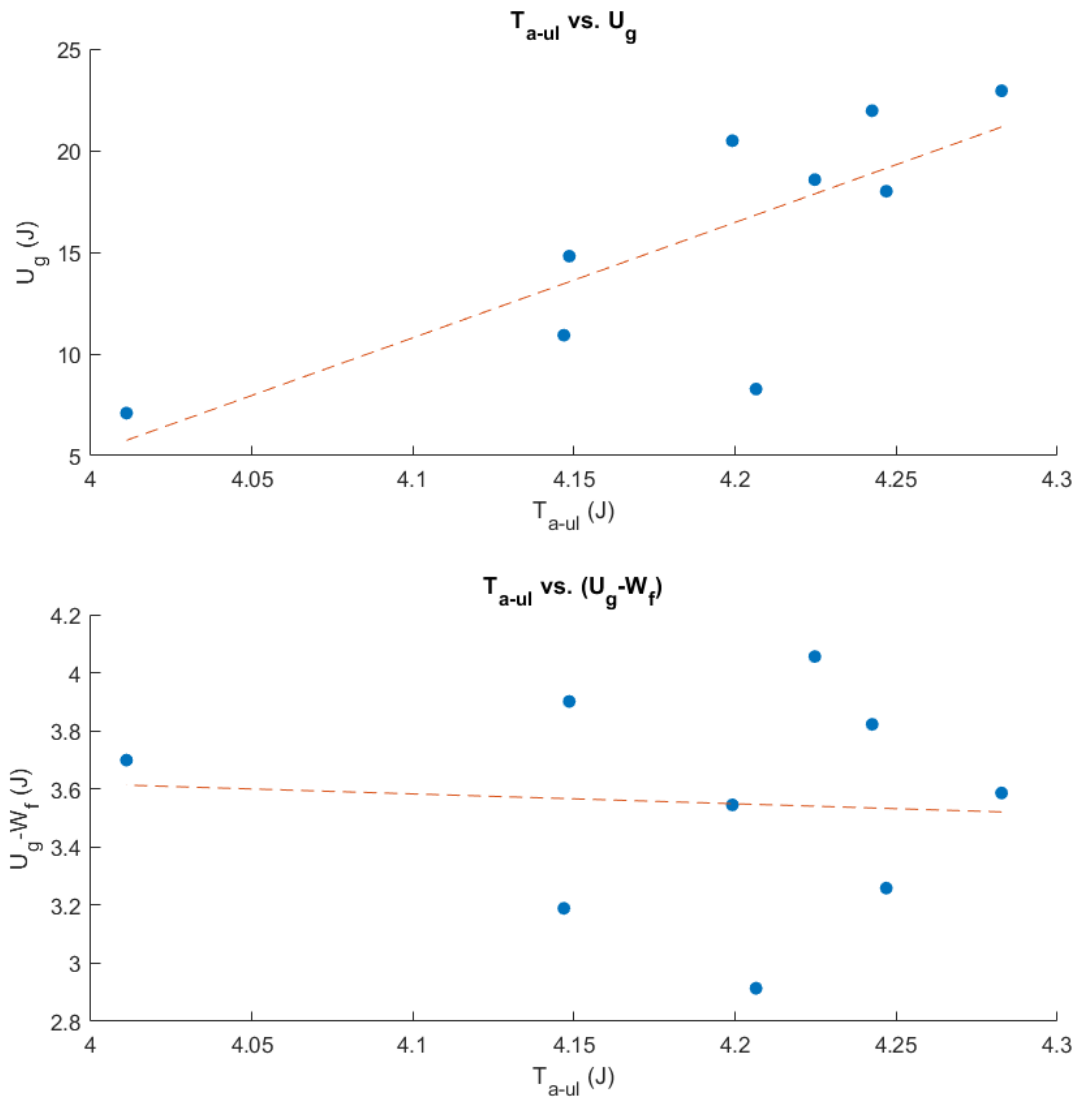


Figure 5.11: T_{a-ul} as performance indicator without (above) and with (below) traction adjustment

Chapter 6

Conclusion

In this work, a procedure for the calculation of three performance indicators, T_a , T_{a-COM} and T_{a-ul} based on a vehicle dynamic model is developed. Beginning with a minimum coordinate representation of the vehicle and the set of forces acting upon it, this model is brought to the impulse-momentum level and discretized using the moments immediately before and after the onset of contact. A linear complementarity problem based on this model is set up and solved to identify the active contacts at the moment of impact. This set of active contacts is used in combination with the mass matrix of the vehicle to isolate the admissible and constrained sub-spaces of motion, from which the performance indicators are derived. A 4-limbed wheel-leg hybrid robot physical test platform is designed and constructed to study the relationship of these performance indicators with obstacle negotiation ability.

Close up video of the wheel-ground contact points is analyzed to validate the LCP solution which predicts the set of active contacts at the onset of contact. High-speed video, encoder values and current measurements are analyzed for 45 slope negotiation experiments across 3 obstacle angles using a neutral, maximum T_a and minimum T_a robot configuration. This analysis shows a strong relationship between T_{a-COM} and maximum obstacle height travelled,

and between T_a and negotiation ability adjusted for the effect of wheel traction. T_{a-ul} shows a weaker relationship with obstacle height traversed, and no relationship with traction-adjusted traversal. These indicators can be used at the design or trajectory planning stage as well as in operational control to improve the mobility of wheeled vehicles travelling at speed without requiring detailed forward dynamics simulations. Analysis of the full maneuver results has shown that a significant factor in the effectiveness of the admissible kinetic energy as performance indicator is in reducing the work done by the obstacle constraints during motion after contact. Therefore, it may be effective to actuate the vehicle suspension joints as it scales a slope so that admissible kinetic is always maximized as the terrain angles relative to the vehicle change. This may be more effective on curved terrain. These indicators can also improve predictions of a given vehicle's ability to negotiate sloped terrain, allowing more optimal path planning on sloped terrain, or reduce required actuator energy on missions where power is limited.

6.1 Suggestions for Future Work

Further work may begin by improving the instrumentation available on the test platform. Altering the data collection system to increase the collection rate would both increase the fidelity of experiments similar to those that have already been performed, and additionally allow integration of the contact force sensor readings. This improvement would however require the construction of a custom data collection system, which was beyond the scope of this project. A higher data collection rate may also provide IMU readings at a sufficiently high frequency so they can be integrated to provide an additional estimate of robot speed and orientation. Current sensors added to the joint actuators would lead to a more accurate assessment of the total amount of work done on the environment during an

obstacle negotiation maneuver.

Much of the error in the motion analysis was not due to lack of information provided by the high speed camera, but rather a lack of precision of the object tracking software. Using a more sophisticated custom or off the shelf motion tracking solution may give sufficiently consistent results that the admissible kinetic energy can be validated directly. A different approach to detect such small displacements, such as an IR tracking camera may be necessary, if image analysis remains insufficiently precise. These more precise tracking methods may also improve the estimate of impact time, and therefore non-contact impulses, which can be used to refine the solution of the LCP.

In addition to re-conducting similar experiments to those outlined in this thesis with the improvements listed above, two main options are available. The effectiveness of online adaptation, as described previously, can be compared to that of a constant configuration. This online adaptation may only show an improvement on more complex obstacles than the flat slope used in this work. Additionally, this robot was designed with a suspension differential which was left locked. For future experiments, it can be unlocked, and the usefulness of the outlined performance indicators can be assessed on uneven terrain, with an added unactuated degree of freedom. Experiments along these lines would require modification of the simulation to account for the differential and non-symmetric ground constraints. An extra encoder can be installed on the main differential shaft to provide the position of each suspension sub-assembly throughout the maneuver.

Bibliography

- [1] Z. Hongbiao, Y. Liu, W. Wang, and Z. Du, “Obstacle negotiation analysis of track-legged robot based on terramechanics,” *Industrial Robot: the international journal of robotics research and application*, vol. 48, pp. 812–822, Jan. 2021.
- [2] K. Turker, “Step climbing behaviour for a wheeled quadruped robot,” Master’s thesis, McGill University, 2012.
- [3] F. Cordes, F. Kirchner, and A. Babu, “Design and field testing of a rover with an actively articulated suspension system in a Mars analog terrain,” *Journal of Field Robotics*, vol. 35, no. 7, pp. 1149–1181, 2018.
- [4] M. Azkarate, M. Zwick, J. Hidalgo-Carrio, R. Nelen, T. Wiese, L. Joudrier, and G. Visentin, “FIRST EXPERIMENTAL INVESTIGATIONS ON WHEEL-WALKING FOR IMPROVING TRIPLE-BOGIE ROVER LOCOMOTION PERFORMANCES,” in *13th ESA Workshop on Advanced Space Technologies for Robotics and Automation*, p. 8, 2015.
- [5] B. Ghotbi, *Performance evaluation and dynamics of rovers for planetary exploration*. PhD thesis, McGill University, 2015.

-
- [6] R. Lindemann, D. Bickler, B. Harrington, G. Ortiz, and C. Voothees, “Mars exploration rover mobility development,” *IEEE Robotics & Automation Magazine*, vol. 13, pp. 19–26, June 2006.
- [7] S. V. Sreenivasan and B. H. Wilcox, “Stability and traction control of an actively actuated micro-rover,” *Journal of Robotic Systems*, vol. 11, no. 6, pp. 487–502, 1994.
- [8] B. Ghotbi, F. González, J. Kövecses, and J. Angeles, “Mobility evaluation of wheeled robots on soft terrain: Effect of internal force distribution,” *Mechanism and Machine Theory*, vol. 100, pp. 259–282, June 2016.
- [9] T. Thuerer, A. Krebs, R. Siegwart, and P. Lamon, “Performance comparison of rough-terrain robots—simulation and hardware,” *Journal of Field Robotics*, vol. 24, no. 3, pp. 251–271, 2007.
- [10] K. Iagnemma, A. Rzepniewski, S. Dubowsky, and P. Schenker, “Control of Robotic Vehicles with Actively Articulated Suspensions in Rough Terrain,” *Autonomous Robots*, vol. 14, pp. 5–16, Jan. 2003.
- [11] Z. Song, Z. Luo, G. Wei, and J. Shang, “A Portable Six-Wheeled Mobile Robot With Reconfigurable Body and Self-Adaptable Obstacle-Climbing Mechanisms,” *Journal of Mechanisms and Robotics*, vol. 14, Mar. 2022.
- [12] K. Skonieczny and G. M. T. D’Eleuterio, “Improving Mobile Robot Step-Climbing Capabilities With Center-of-Gravity Control,” in *ASME 2010 International Design Engineering Technical Conferences and Computers and Information in Engineering Conference*, pp. 1531–1538, American Society of Mechanical Engineers Digital Collection, Mar. 2011.

- [13] Z. An, Z. Zhou, D. Li, and Z. Gao, “Dynamic behaviours of an integrated crawler mobile parallel robot in obstacle-crossing,” *Nonlinear Dynamics*, vol. 111, pp. 16939–16962, Aug. 2023.
- [14] Z. Y. Cai Xin, Zhong Yi and M. Yan, “Optimization on design parameters of road longitudinal slope based on truck dynamics,” in *Green, Smart and Connected Transportation Systems*, pp. 1325–1342, 2020.
- [15] Z.-H. Dong, F.-Y. Ni, S.-M. Liu, and X. Liu, “Heavy truck climbing speed on long and steep longitudinal slope section,” *Chang’an Daxue Xuebao (Ziran Kexue Ban)/Journal of Chang’an University (Natural Science Edition)*, vol. 34, no. 3, pp. 23 – 27, 2014. Function modeling;Heavy truck;Long and steep longitudinal slope;Power transmission systems;Road engineering;Torque characteristic;Vehicle speed;Vertical direction;.
- [16] S. J. Pan Guanting, Yang Fuzeng and L. Zhijie, “Analysis and test on the climbing and obstacle-crossing performance of small mountain crawler tractors,” *Transactions of the Chinese Society for Agricultural Machinery*, vol. 51, no. 9, pp. 374–383, 2020.
- [17] W. Nowac, F. Gonzalez, S. MacMahon, and J. Kovecses, “Performance Indicators for Wheeled Robots Traversing Obstacles,” *IEEE Robotics and Automation Letters*, vol. 5, pp. 2881–2888, Apr. 2020.
- [18] S. MacMahon, “Modelling and Contact Analysis of Planetary Exploration Rovers,” Master’s thesis, McGill University, 2016.
- [19] P. Jarrault, C. Grand, and P. Bidaud, “Large obstacle clearance using kinematic reconfigurability for a rover with an active suspension,” in *Emerging Trends in Mobile Robotics*, pp. 114–121, WORLD SCIENTIFIC, Aug. 2010.

- [20] “Schaeffler’s Autonomous Mobile Robot DEX awarded with “Red Dot: Best of the Best”” <https://www.schaeffler.com/en/media/press-releases/press-releases-detail.jsp?id=87850753>.
- [21] H. Jiang, G. Xu, W. Zeng, F. Gao, and K. Chong, “Lateral Stability of a Mobile Robot Utilizing an Active Adjustable Suspension,” *Applied Sciences*, vol. 9, p. 4410, Oct. 2019.
- [22] I. Zournatzis, K. Koutsoukis, K. Machairas, A. Kecskeméthy, and E. Papadopoulos, “Maera: A hybrid wheeled-legged robot designed for research and education,” 01 2021.
- [23] A. Laurenzi, E. M. Hoffman, and N. G. Tsagarakis, “Quadrupedal walking motion and footstep placement through Linear Model Predictive Control,” in *2018 IEEE/RSJ International Conference on Intelligent Robots and Systems (IROS)*, (Madrid), pp. 2267–2273, IEEE, Oct. 2018.
- [24] J.-M. Jehanno, A. Cully, C. Grand, and J.-B. Mouret, “Design of a Wheel-Legged Hexapod Robot for Creative Adaptation,” in *CLAWAR 17th International Conference on Climbing and Walking Robots*, (Poznan, Poland), pp. 267–276, July 2014.
- [25] Y. Yamamoto, Y. Zhao, and K. Mizuno, “Analysis of normal and tangential restitution coefficients in car collisions based on finite element method,” *International Journal of Crashworthiness*, July 2022.
- [26] K. G. Murty, “On the number of solutions to the complementarity problem and spanning properties of complementary cones,” *Linear Algebra and its Applications*, vol. 5, no. 1, pp. 65–108, 1972.
- [27] M. Tsatsomeros, “Lecture notes on matrices with positive principal minors: Theory and applications,” 2017.

-
- [28] J. Kövecses. "Redundancy: A Challenge in Dynamics Simulation", *2018 IEEE International Conference on Simulation, Modeling, and Programming for Autonomous Robots (SIMPAN 2018)*, Brisbane, Australia, May 16-19, 2018,.
- [29] J. Kövecses, "Dynamics of Mechanical Systems and the Generalized Free-Body Diagram—Part I: General Formulation," *Journal of Applied Mechanics*, vol. 75, Aug. 2008.

Appendix A

Design Calculations

A.1 Joint Actuators

The torque requirements for the joint actuators are calculated assuming they must be able to support the weight of the robot under static conditions when the links are fully extended using no more than half of their stall torque. This case is illustrated in A.1 with the mass of the robot $m_r = 6.797\text{kg}$ and the fully extended length of the robot $L_r = 70\text{cm}$. The reactions

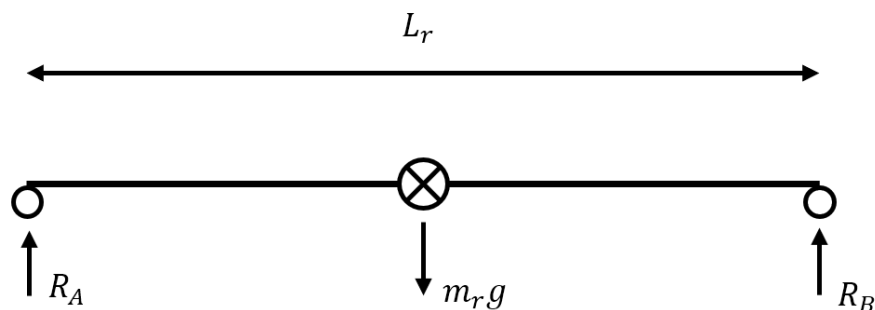


Figure A.1: Diagram of rover at full extension

R_a and R_b can be calculated as

$$\sum F = R_a + R_b - m_r g = 0 \quad (\text{A.1})$$

$$\sum M_A = R_B L_r - m_r L_r / 2 = 0 \quad (\text{A.2})$$

$$R_A = R_B = \frac{m_r g}{2} = 33.34N \quad (\text{A.3})$$

Individual joint torque requirements can then be calculated by summing the moments at a cut through each joint under static conditions, following Fig. A.2. For simplicity, the centres of mass are shown as being in the center of each link. The actual joint-COM L_{xg} displacements are used where this assumption does not hold. T_b , M_b , m_b and L_b refer to the bicep link, while T_f , M_f , m_f and L_f refer to the forearm.

$$\sum M_e = T_e - R_A L_f + m_f g L_{fg} = 0 \quad (\text{A.4})$$

$$\sum M_b = T_b - R_A (L_f + L_b) + m_f g (L_f + L_{bg}) + m_b g (L_{bg}) = 0 \quad (\text{A.5})$$

$$T_e = 3.29Nm, T_b = 6.47Nm \quad (\text{A.6})$$

As this calculation is performed using a 2-D simplification of the robot, the calculated loads are shared between the two sides of the rover. The required torque is therefore divided in two, and then multiplied by two using the maximum power point as maximum operating point to generate the stall torque requirement. Adjustment and steering motor requirements are generated using the same procedure with an extended model and a link length of 5cm for the adjustment motor and a wheel radius of 5cm for steering.

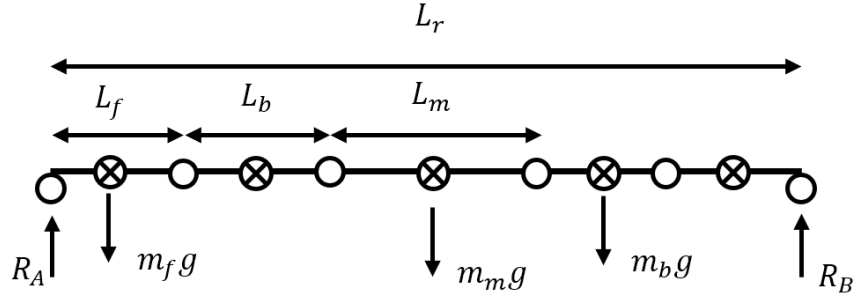


Figure A.2: Diagram of rover bodies at full extension

A.2 Slope Driving

Drive motors were chosen assuming the robot must be able to maintain its speed on a 40° slope, and traverse flat ground at up to 2m/s. The torque requirement is calculated first by referring to Fig. A.3. F_g is equal to the weight of the rover, F_f is the sum of wheel-ground friction forces, and F_n is the sum of normal forces. The drive forces can be calculated as follows, with x axis parallel to slope and y axis perpendicular to slope.

$$\sum F_x = F_f - F_g \sin(\theta) = 0 \quad (\text{A.7})$$

$$F_f = m_r g \sin\left(\frac{\pi}{4}\right) = 42.8N \quad (\text{A.8})$$

Assuming equal torque distribution between wheels, each motor should have be able to produce $42.8/4 = 10.7N$ at its wheel edge, while travelling at 2m/s. This translates to a power requirement of $10.7 * 2 = 21.4W$. Using a 4.5cm radius wheel, this is a torque requirement of $0.045 * 10.7 = 0.482Nm$ or 4.92 kg-cm. With the same size wheel, travelling at 2m/s requires a rotational speed of 424 rpm. It can be verified that the 612 rpm HD planetary gearmotor fulfills this requirement in combination with a 9cm diameter wheel

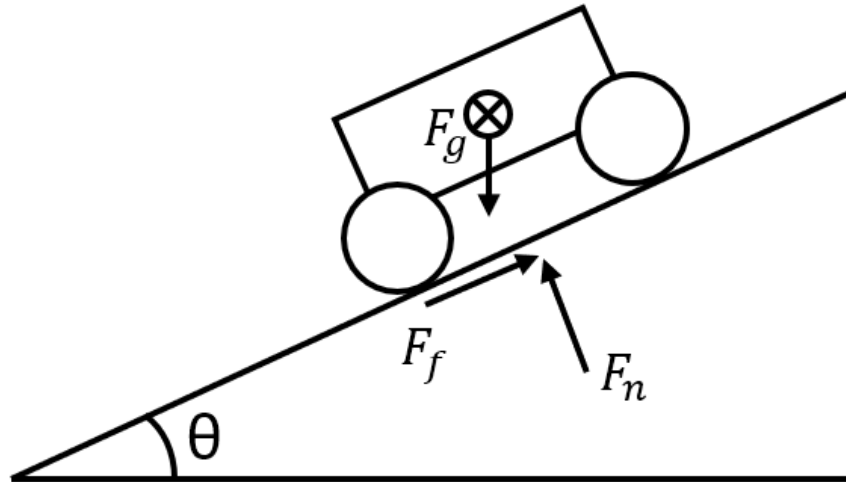


Figure A.3: Simplified robot climbing slope at constant speed

using its stall torque of 16 kg-cm and free speed of 612 rpm. Assuming constant torque and speed constants, at 424rpm the motor is at $424/612 = 69\%$ of its maximum speed, and can therefore output $(1 - 0.69) * 16 = 4.92\text{kg} - \text{cm}$ of torque which fulfills the requirements.

When traversing a slope, the weight distribution and therefore the required torque across all wheels may often be uneven, depending primarily on the position of the center of mass. A significant motor torque safety factor is therefore left, with a 66% torque increase possible before the maximum power point is reached. The worst possible case is all robot weight resting on two wheels, doubling the torque required which would still leave the motors below stall and likely would not cause damage for the short experiment run time of 2-3s.

A.3 Stress Analysis

The main candidates for stress analysis are the forearm and bicep links, the differential shaft and the suspension attachment member. These parts all carry forces from the suspension

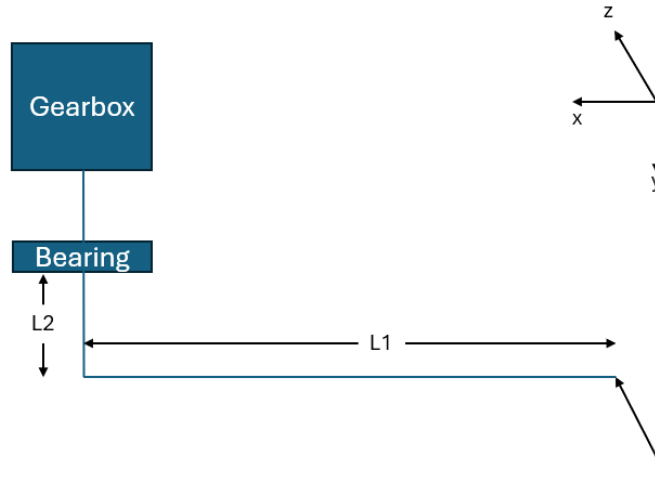


Figure A.4: Differential load case

and need to occupy a compact space. The main robot frame, alternatively, needs only to carry all electrical components, as the differential mechanism serves as the main connection point for each side of the suspension.

A.3.1 Differential Shaft

A differential mechanism must be chosen to connect each side of the robot suspension, and allow them to rotate in countervailing directions to one another. Off-the-shelf versions are available, using 6, 8 and 10mm shafts. Stress calculations are performed to determine if one of these versions is sufficiently strong. Otherwise, a custom gearbox will be constructed, which will increase design time and cost. The load case is a conservative scenario where half the weight of the robot is applied to only one wheel in fully outstretched configuration, shown in Fig. A.4. At its critical point (the edge of the shaft at the support bearing) with $F = m_r g / 2 = 33.34N$, the shaft undergoes $T = L_1 F = 15Nm$ of torsion and $M =$

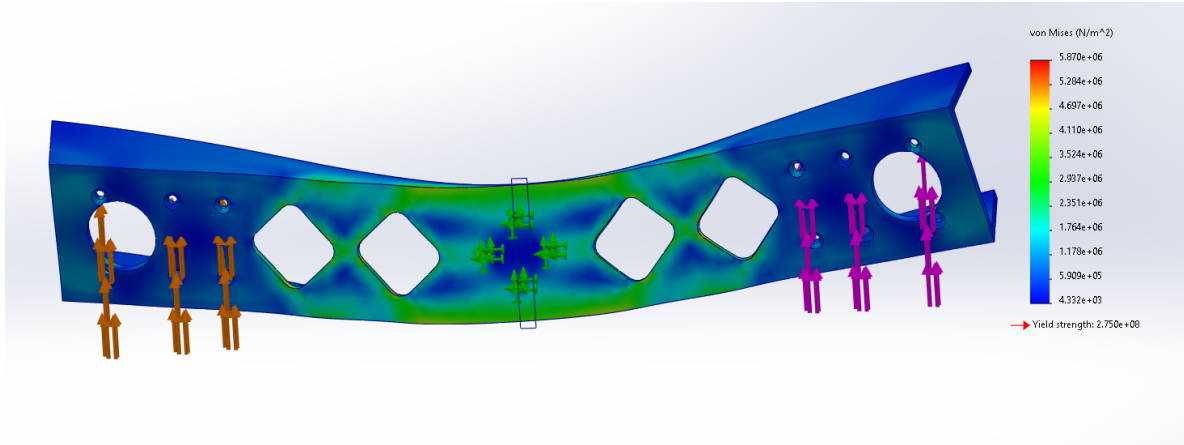


Figure A.5: Suspension attachment FEA

$L_2F = 3.6Nm$ of bending moment. Direct shear is 0 at that point, and normal stress is comparatively minor. The material is 45 carbon steel with a yield stress of 310MPa, and therefore required radius for a safety factor of $N = 1.5$ can be calculated according to Von Mises failure criterion as follows.

$$\sigma_{12} = \frac{T}{J} = \frac{2T}{\pi r^3} \quad (\text{A.9})$$

$$\sigma_{11} = \frac{My}{I} = \frac{4M}{\pi r^3} \quad (\text{A.10})$$

$$\sigma_v = \sqrt{\left(\frac{4M}{\pi r^3}\right)^2 + 3\left(\frac{2T}{\pi r^3}\right)^2}; \text{ Plane stress with } \sigma_{22} = 0 \quad (\text{A.11})$$

With $r = 3 * 10^{-3} \text{ N} = 0.49$, $r = 4 * 10^{-3} \text{ N} = 1.16$ and $r = 5 * 10^{-3} \text{ N} = 2.25$. Therefore, the 10mm diameter shaft is chosen.

A.3.2 Finite element analysis

The remaining structural members are analyzed using finite element analysis in SolidWorks, due to more complex geometry. The load case follows the calculations in A.1. The material

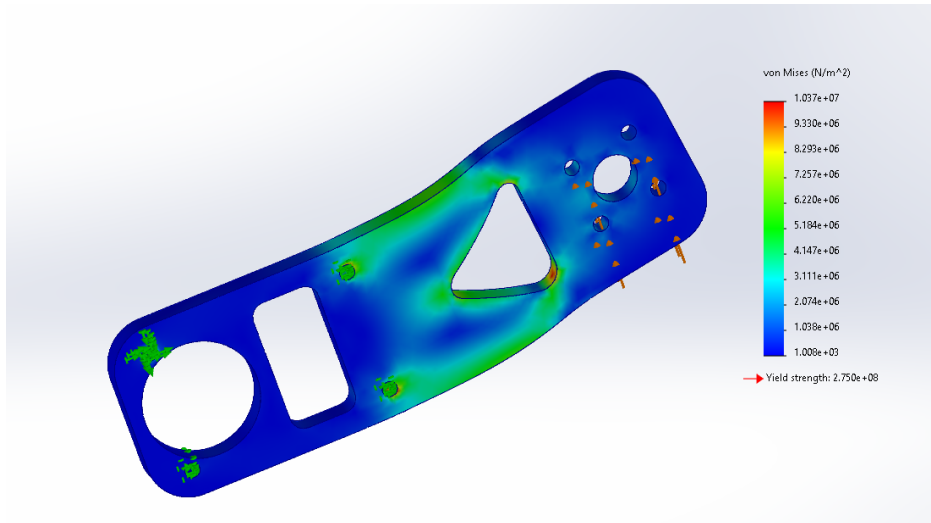


Figure A.6: Shoulder link FEA

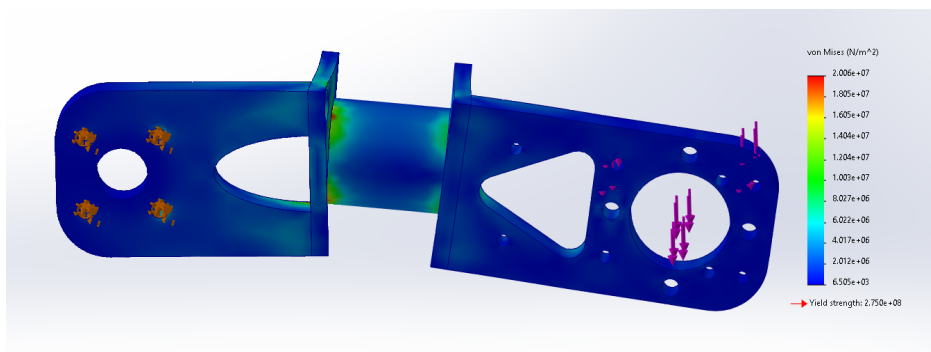


Figure A.7: Bicep link FEA

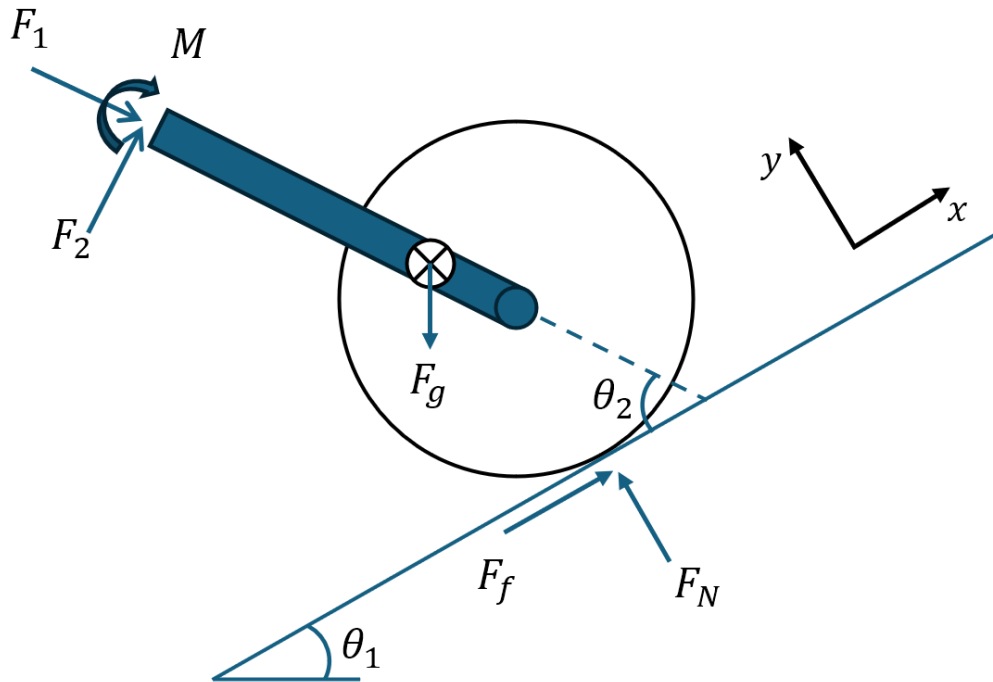


Figure A.8: Free body diagram of robot between elbow joint and ground

is 6061 Al T6 with a yield strength of 275MPa. The suspension attachment member is constructed from u-channel as a flat bar of sufficient strength would be impractically heavy. Each member is fixed at the bolt holes of the upper joint, and load is applied divided amongst the bolt holes of the lower joint. Loads are applied in a direction such that buckling is not a significant factor.

A.4 2D Force Sensor

Consider Fig. A.8 which illustrates the forces acting on the section of the robot between the force sensor in the forearm link and the ground. This consists of the bicep, the force sensor, the wheel and the drive motor, for a total of about $m=0.54$ kg. The force F_1 is

known and measured by the load cell, and the moment M can be measured from the elbow actuator, but F_2 is unknown. The angle θ_1 is known from obstacle geometry, while θ_2 is slightly harder to calculate. On flat ground, it is known from the robot configuration, but otherwise must be calculated using footage from a high speed camera or some other marker of robot orientation. The distance between bicep joint and wheel centre r_{bc} , wheel radius r_w and sub-assembly inertia I are known as well. The friction force F_f and normal force F_N can then be calculated as follows:

$$\sum F_x = ma_x = F_f - mg\sin(\theta_1) + F_1\cos(\theta_2) + F_2\sin(\theta_2) \quad (\text{A.12})$$

$$\sum F_y = ma_y = F_N - mg\cos(\theta_1) - F_1\sin(\theta_2) + F_2\cos(\theta_2) \quad (\text{A.13})$$

$$\sum M_z = I\alpha_z = M + F_N\sin(\theta_2)r_{bc} + F_f\sin(\theta_2)(r_{bc} + r_w) \quad (\text{A.14})$$

This results in a solvable set of equations for F_f , F_N and F_2 , assuming the accelerations a_x , a_y and α can be measured. The mass of this sub-assembly is low compared to the rest of the robot, so the accelerations may be ignored for a moderate but not negligible error, especially on even ground where acceleration is not predicted to be high. Using a 3- or 6-axis force sensor would not remove the inertial error factors, or eliminate the calculation of θ_1 or θ_2 but would likely improve accuracy by allowing M to be measured directly instead of calculated using motor values. Additionally, knowing F_2 would reduce the required number of equations to 2, meaning that the most error prone of a_x , a_y and α_z need not be used. This set of calculations was not implemented due to measurement rate issues which prevented force measurements being considered in the impact analysis.

Appendix B

Design Drawings

B.1 Machine Drawings

B.1.1 Frame Parts

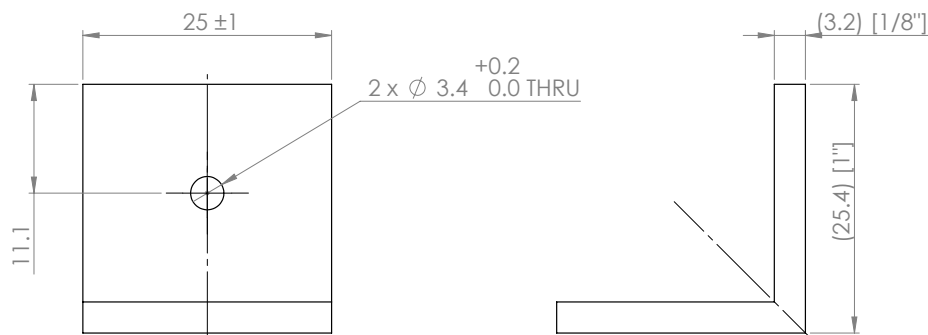


Figure B.1: Frame bracket

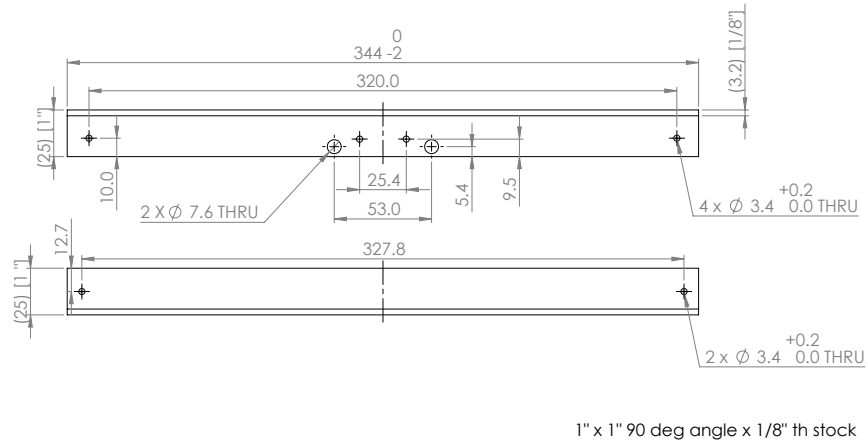


Figure B.2: Long frame bar

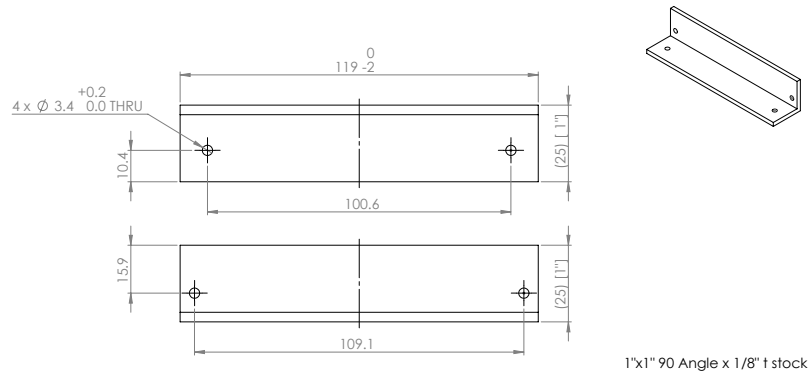


Figure B.3: Short frame bar

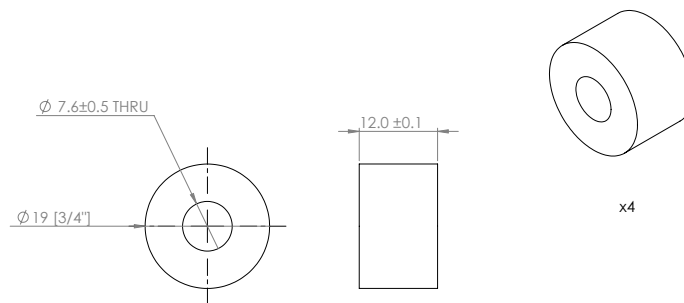
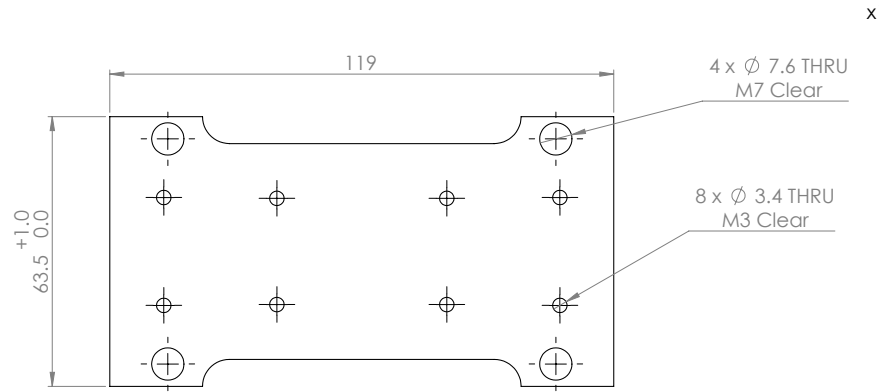


Figure B.4: Spacer for pillow-block mounting



3.175 mm plate [1/8"] leave as supplied

Figure B.5: Frame-differential attachment plate

B.1.2 Suspension

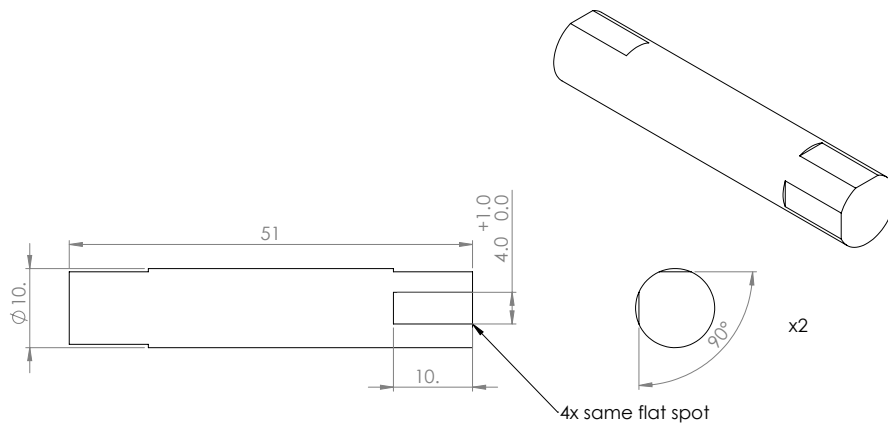


Figure B.6: Differential shaft extension

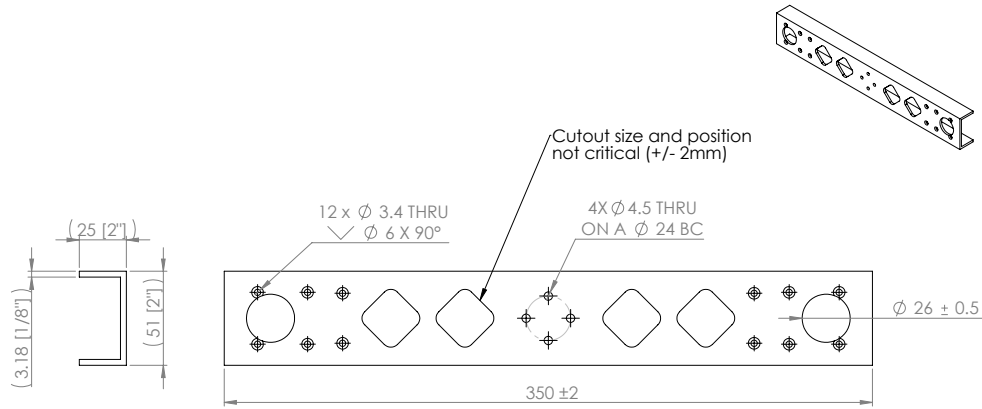


Figure B.7: Suspension attachment member

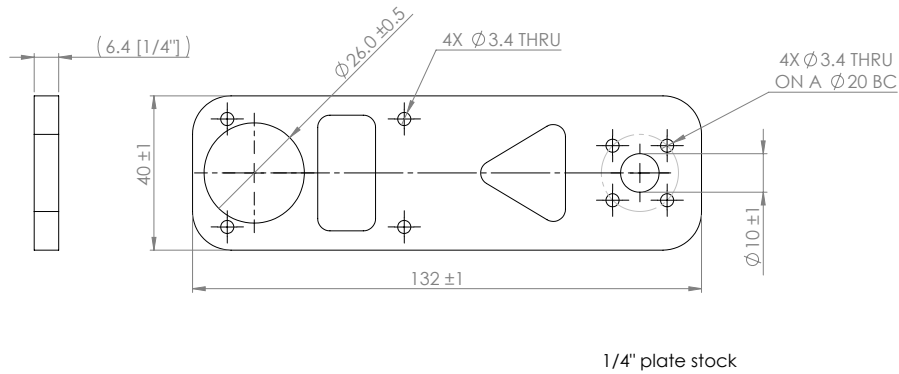


Figure B.8: Shoulder link

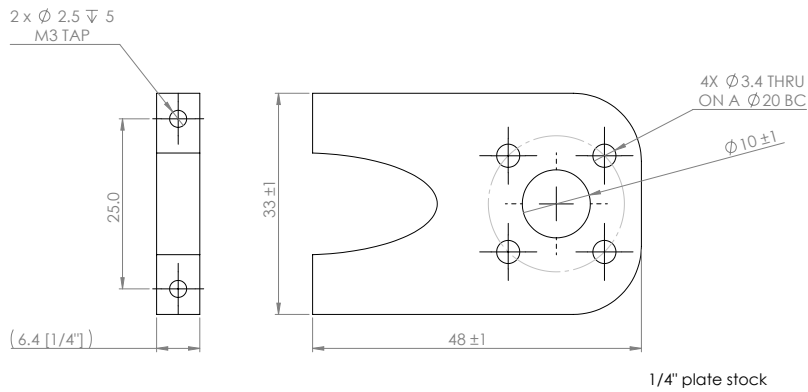


Figure B.9: Upper load cell link

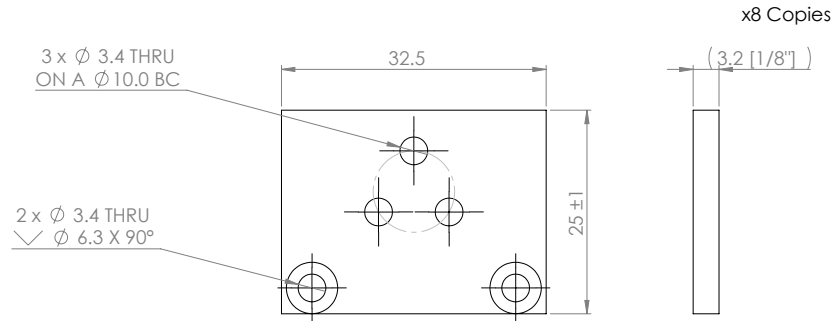


Figure B.10: Load cell attachment plates

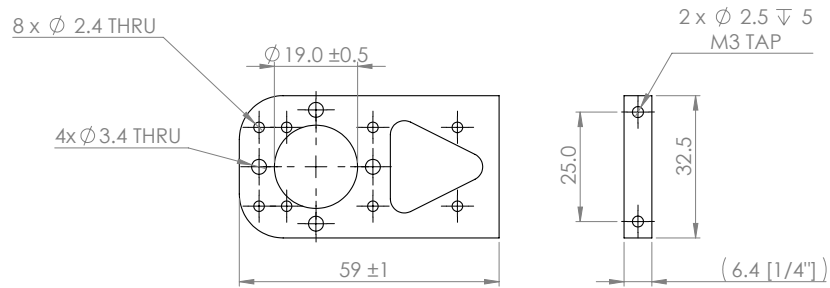
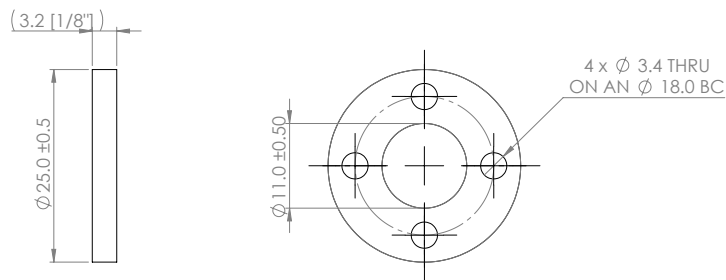


Figure B.11: Lower load cell link



1/8" delrin plate

Figure B.12: Large actuator spacer

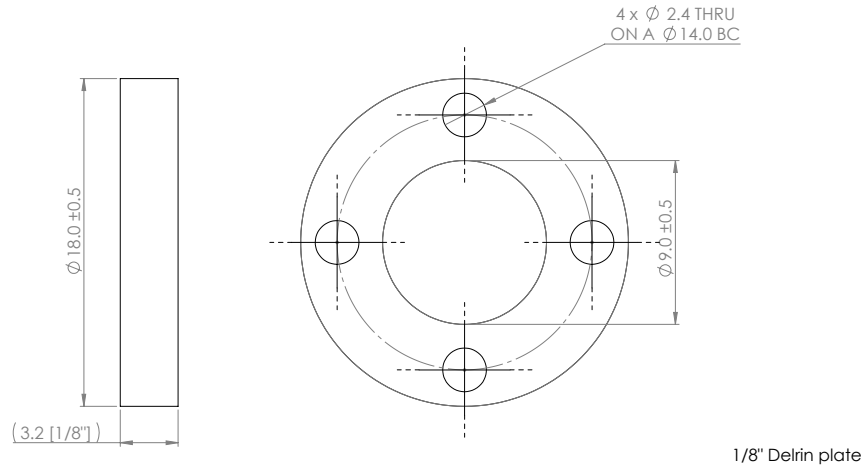


Figure B.13: Small actuator spacer

B.1.3 Modular Motor Mounts

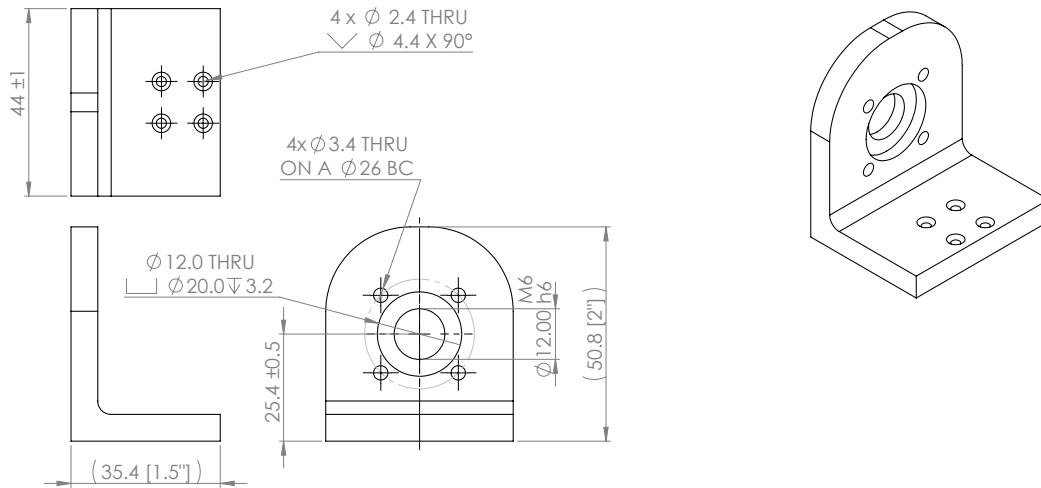


Figure B.14: Adjuster motor mount

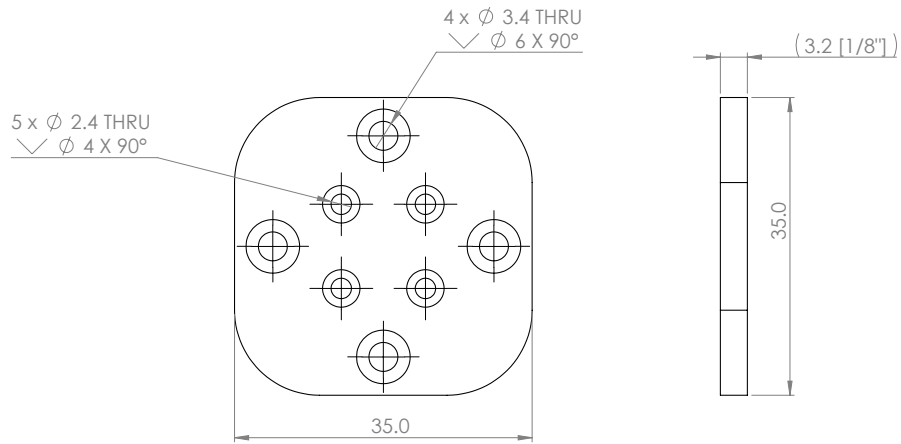


Figure B.15: Actuator attachment plate

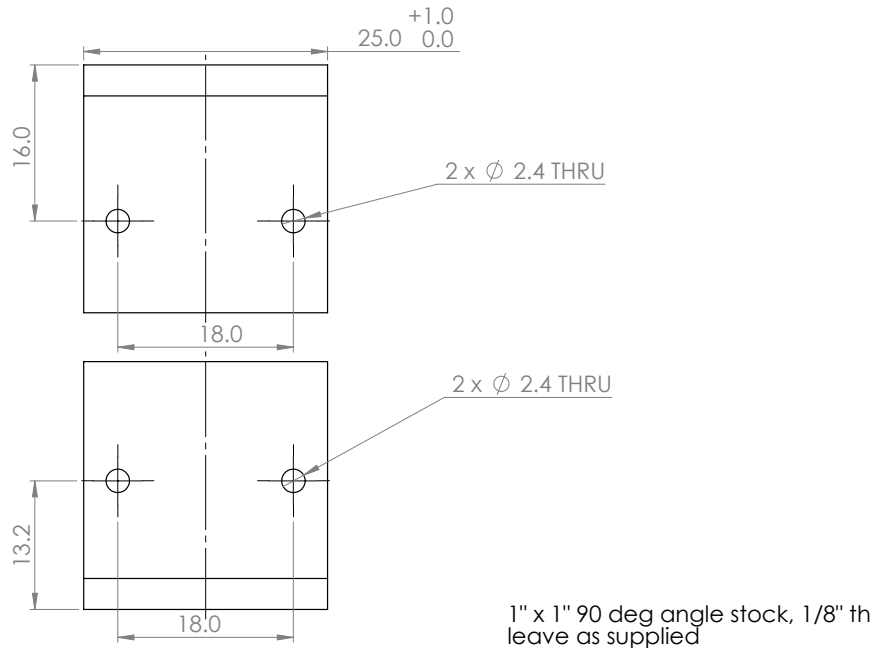


Figure B.16: Rear actuator attachment plate

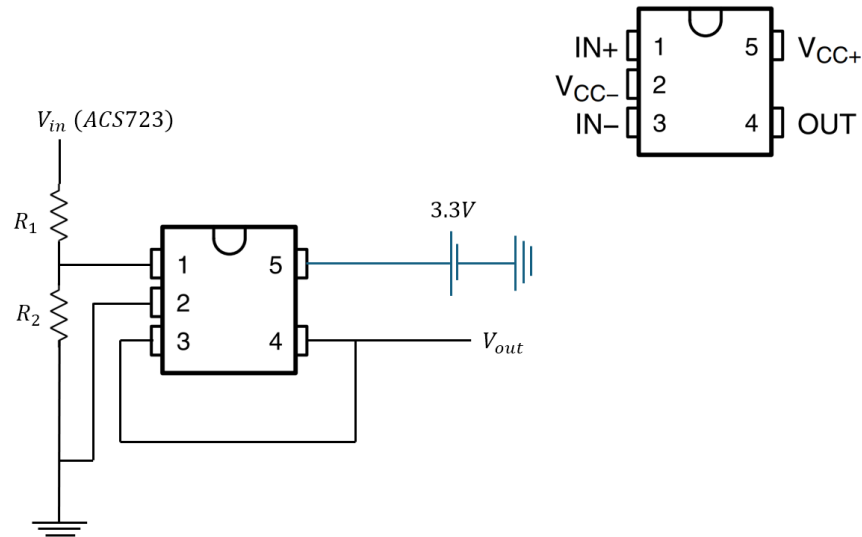


Figure B.17: Current sensor circuit diagram

B.2 Current Sensor Circuit

The selected current sensor, ACS723, has a measurement range of $\pm 5\text{A}$. With a sensitivity of 0.400mV/A , the output of the sensor will be $\pm 2\text{V}$, centered at $V_{in}/2$. The ACS723 is powered by the 5V pin of the raspberry Pi, and therefore has a possible output of $[0.5\text{V } 4.5\text{V}]$. The purchased ADS1015 analog-digital converter breakout board has a sufficient measurement range ($[\text{GND } V_{in}] = [0\text{V } 5\text{V}]$) and sufficient inputs (4) to record each current reading. However, though it is part of the Sparkfun Quic ecosystem, this breakout board was not recognized by the Artemis master board, and therefore could not be used. The Artemis board has four analog inputs, but with a measurement range of only $0\text{-}2\text{V}$. Therefore, a voltage divider with op-amp for signal isolation was constructed, to ensure that current readings could still be recorded by the same data collection system as IMU readings and load cell data. This voltage divider circuit is shown in Fig. B.17 using a TLV2362 op-amp. The divider ratio is $\frac{V_{out}}{V_{in}} = \frac{R_2}{(R_1+R_2)} = \frac{2}{5}$, giving a value of $R_1 = 33\text{k}\Omega$ and

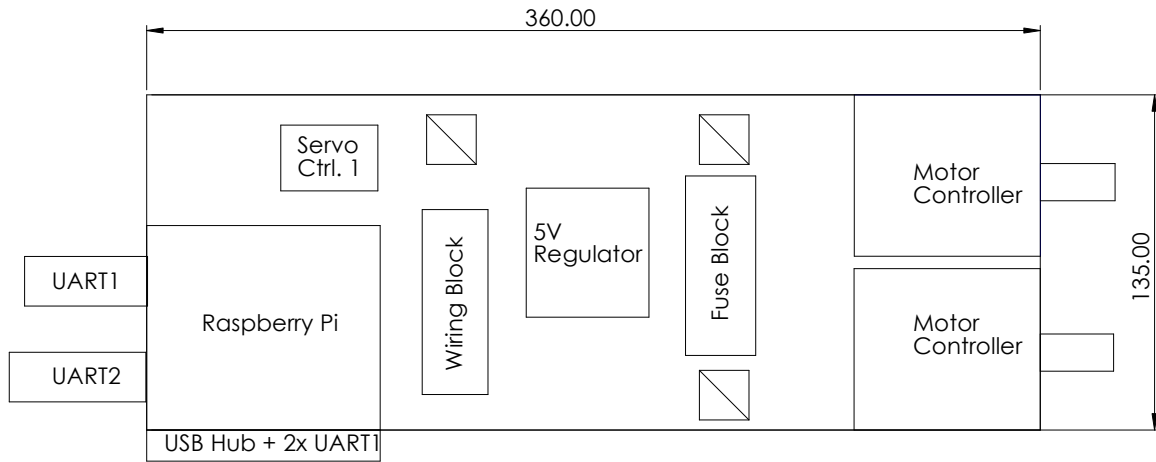


Figure B.18: Component diagram-Main level (mm)

$R_2 = 22k\Omega$ according to available resistors.

B.3 Main Body Layout

The layout of components on the main body of the robot is shown to scale in Fig. B.18 and Fig. B.19. The upper level was added for space during the assembly and testing process, as the current dividers and drive motor fuse holder (instead of a system wide fuse) were added to the preliminary design. Additional fuse holders for the joint actuators are mounted to suspension attachment members, to reduce the number of wires going from main body to the rotating suspension. The electrical parts list is shown in Table B.1.

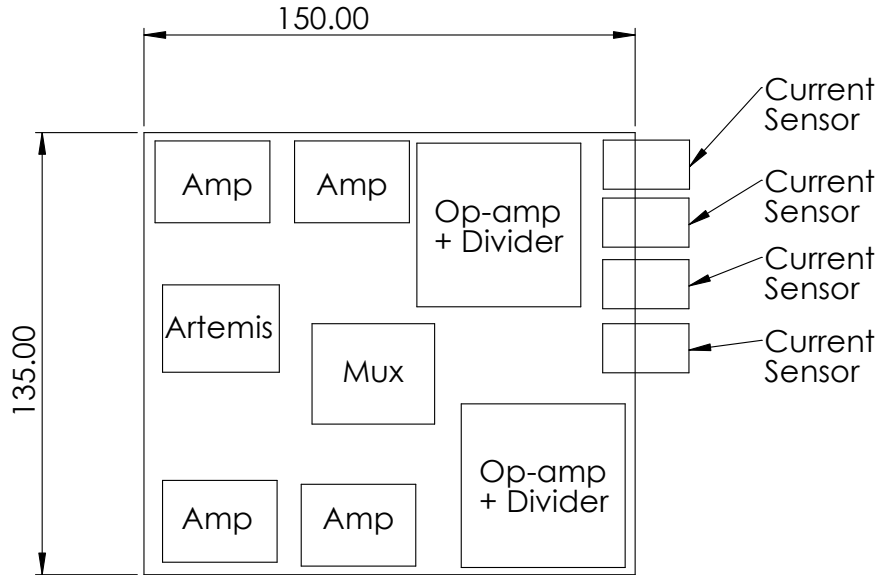


Figure B.19: Component diagram-Upper level (mm)

Component Reference	Part Number	Number
UART1	HerkuleX Servo Manager Serial Cable	1
UART2	SH-U09C5 USB to TTL UART	3
Raspberry Pi	Raspberry Pi 4 8Gb	1
USB Hub	ANKER 4-port USB 3.0 Data Hub	1
Servo Ctrl1	HerkuleX Servo Manager	1
Wiring Block	8 position 15A Terminal Block	1
5V regulator	5V 3A Buck Regulator	1
Fuse Block	4 Place Fuse Block	1
Motor Controller	Sabertooth 12A 6-48V speed controller + Kangaroo Servo Control Unit	2
Artemis	Sparkfun OpenLog Artemis	1
Amp	Qwiic NAU7802 Load Cell Amplifier	4
Mux	Qwiic TCA9548A 8 channel multiplexer	1
Op-amp + Divider	Constructed circuit with TLV2362	2
Current Sensor	ACS723 Breakout	4

Table B.1: List of major electrical components

B.4 Electrical System Diagrams

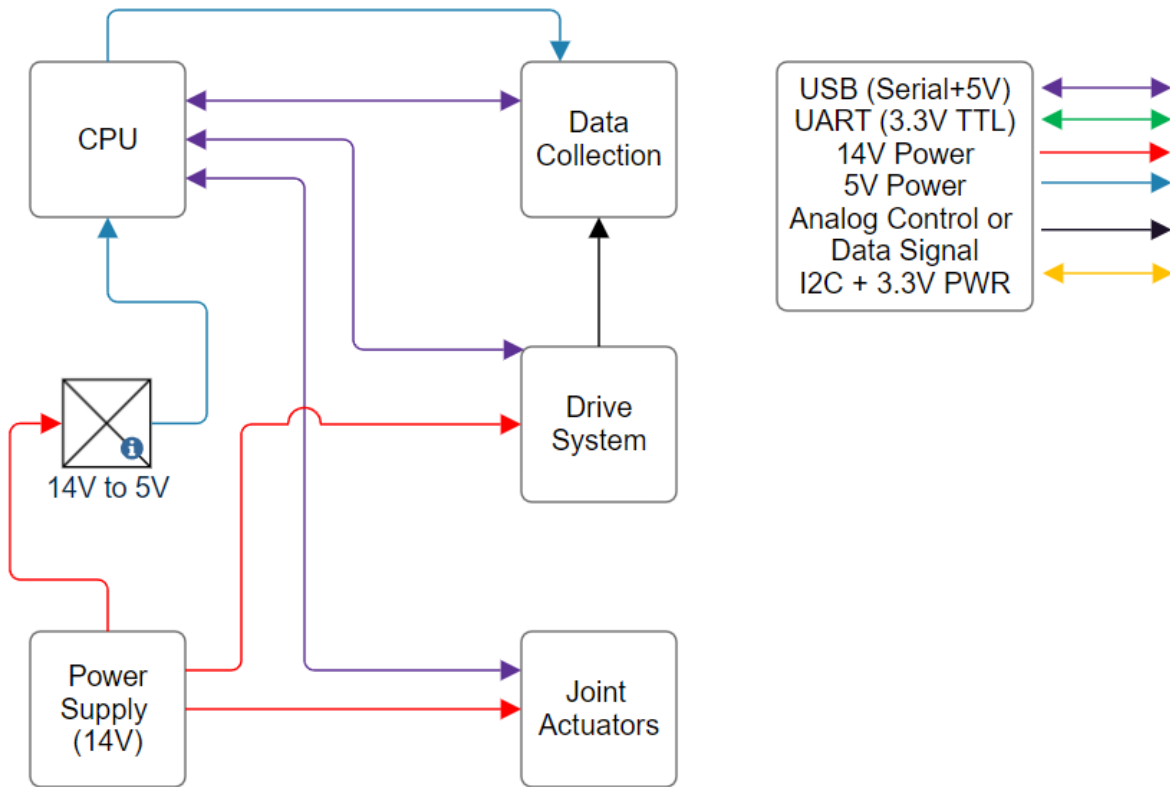


Figure B.20: Electrical system overview

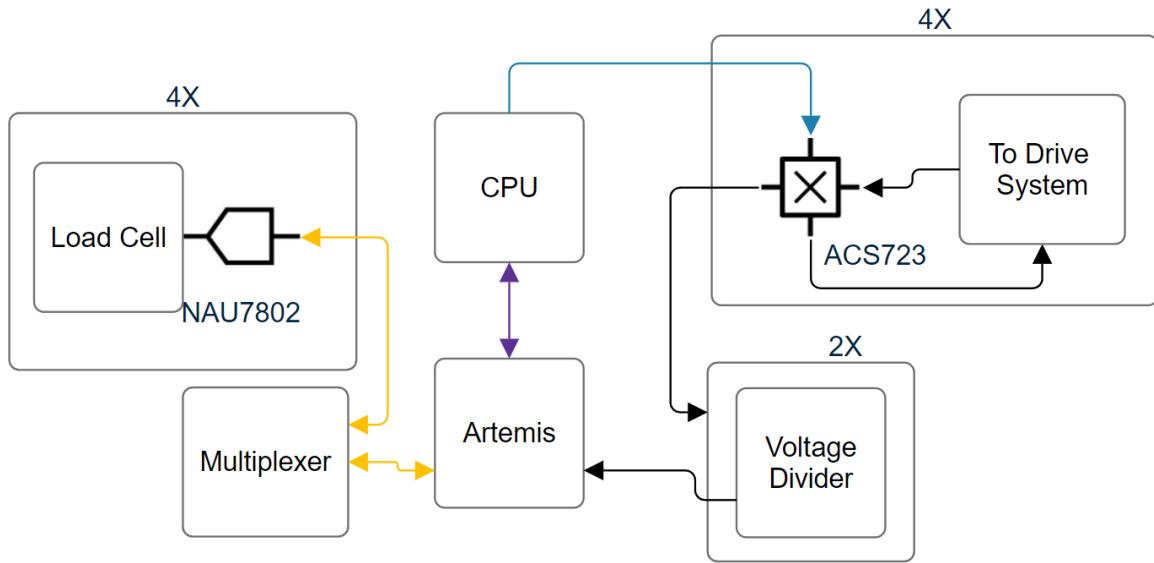


Figure B.21: Data collection system

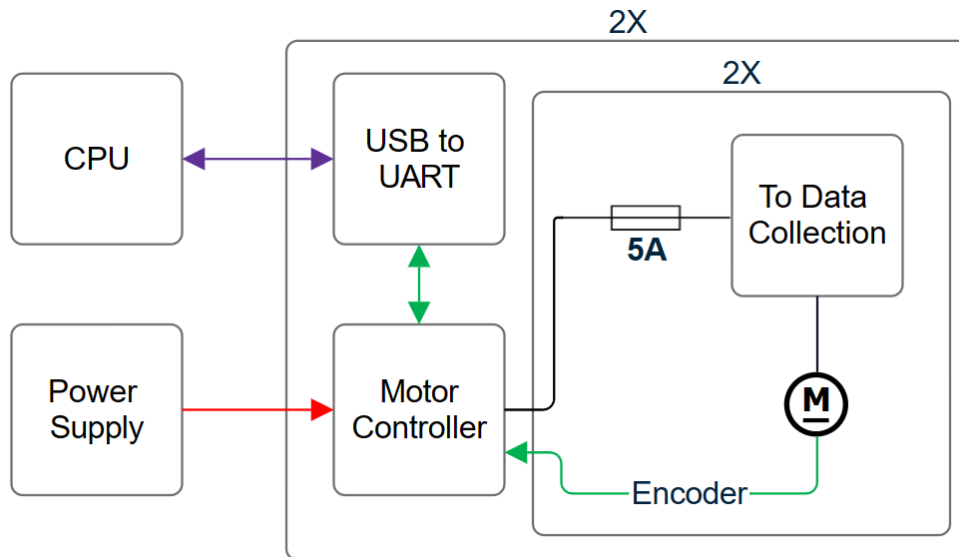


Figure B.22: Drive system

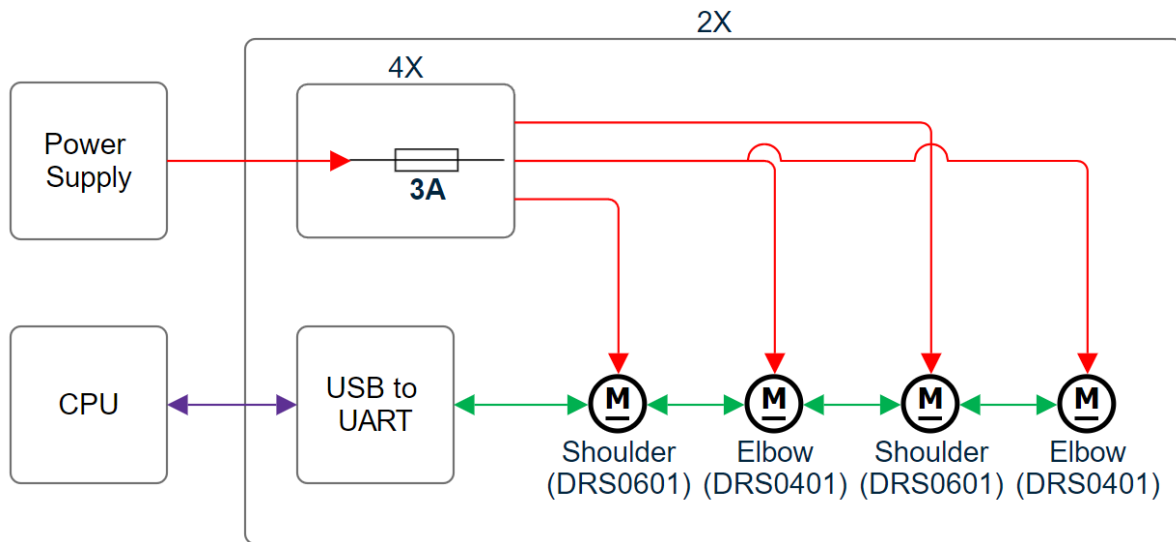


Figure B.23: Actuator system